X-ray Absorption Spectroscopy Studies of Metal and Metal-Oxide Nanocatalysts

by

David A. Do

Submitted in partial fulfillment of the requirements

for the degree of Master of Science

at

Dalhousie University

Halifax, Nova Scotia

November 2020

Table of Contents

List of Tables

List of Figures

Abstract

Nanoparticles have received much attention due to their unique structure and physical and chemical properties compared to their bulk material counterparts, which allow them to be used in a variety of applications, such as imaging, medical applications, and catalysis. As such, close examination of the structure and electronic properties of various nanoparticles is of incredibly high interest.

In this work, X-ray absorption spectroscopy (XAS), supported by other characterization techniques, was used to study the structure and bonding properties of a number of different nanoparticle catalysts. First, a series of W-doped TiO_2 nanoparticles was examined, in order to determine the changes in atomic structure that allowed for the W-TiO_2 4% doping to exhibit greater photothermalcatalytic activity than the other samples. Extended X-ray Absorption Fine Structure (EXAFS) fittings results showed that the dopant W atoms replaced Ti atoms within the lattice, creating Ti vacancies. As the W doping concentration increased to 4%, the Ti vacancies also increased, as did the number of dangling oxygen and oxygen vacancies, which could act as catalytic sites. Formation of WO_3 outside of the lattice at 10% doping was also seen in the fitting results, showing why the 4% sample exhibited greater catalytic activity.

Next, a series of manganese cobalt oxides supported on carbon nanotubes were studied, with XAS results allowing for a clearer picture of the phase transition from a cubic structure to a tetragonal structure as the amount of manganese in the samples increased and the amount of cobalt decreased. $Mn_{1.5}Co_{1.5}O_4$, which contains an equal ratio of Co and Mn, was found to have a dual-phase structure, based on both EXAFS fitting results and linear combination X-ray absorption near-edge structure (LC XANES) fitting. This was unlike the other samples studied, which were either completely cubic phase or tetragonal phase structures, and further understanding of the dual-phase structure would potentially allow for better fine-tuning of the structure of the sample, and as such, its catalytic applications.

Finally, a number of ruthenium nanoparticle samples, both monometallic and bimetallic, were synthesized and supported on three different zeolite supports (Y, beta, and mordenite) with varying concentrations of the ruthenium ion precursor to determine the effect of concentration and support on the local structure and bonding properties. It was found that bimetallic samples of Ru and Pd displayed strong indications of metal core formation, whereas Ru and Co bimetallic samples showed little metal core formation, as seen in the EXAFS fitting results for all samples.

This work highlights the importance of the relationship between the structure of nanoparticles and their properties. X-ray absorption spectroscopy gives a deep understanding of the structure and bonding properties of representative sites of nanoparticles, and by using the information obtained from such studies, a clearer picture of the nanoparticle structure can be formed. These results could lead to further development into tailoring the structure of certain nanoparticles in order to optimize their performance in relevant applications.

List of Abbreviations Used

APS   Advanced Photon Source

BEA   Beta (Zeolite)

CN   Coordination Number

EXAFS   Extended X-ray Absorption Fine Structure

FT   Fourier Transformation

LC   Linear Combination

$Mn_xCo_{3-x}O_4$@NCNTs   Manganese Cobalt Oxide Nanoparticles on Nitrogen-doped

                             Carbon Nanotubes

MOR   Mordenite (Zeolite)

OER   Oxygen Evolution Reaction

ORR   Oxygen Reduction Reaction

PXRD   Powder X-ray Diffraction

SPR   Surface Plasmon Resonance

TEM   Transmission Electron Microscopy

XANES   X-ray Absorption Near-Edge Structure

XAS   X-ray Absorption Spectroscopy

Acknowledgements

Chapter 1: Introduction

1.1   General Background of Nanoparticles

The *nanometer* is a metric unit of length that specifies one-billionth of a meter, or 10^{-9} m. As such, nanoparticles are incredibly small particles with at least one dimension smaller than 100 nm; some nanoparticles display physical properties resembling those of bulk samples when exceeding this length.[1] Nanoparticles, as well as other nanoscale materials, have received considerable attention due to their unique physical and chemical properties compared to those of their respective bulk materials.[2–4] Fundamental studies into the structure, preparation, and properties of such materials is known as nanoscience, and the dedicated research of the technological applications of these materials is known as nanotechnology.[1,2]

There exist many different methods in which to prepare metal nanoparticles, which can generally be classified as either a "top-down" approach or a "bottom-up" approach.[5] Top-down preparation methods are typically physical in nature since they involve breaking down large, bulk matter into smaller pieces to reach a desired form.[6] In contrast, bottom-up methods involve building up metal nanoparticles gradually through chemical synthesis from smaller atoms or molecules.[7] Bottom-up synthesis methods are generally preferred when preparing metal nanoparticles, as such processes allow for much greater control over the size and structure.[8]

The unique physical and chemical properties of nanoparticles can largely be attributed to quantum size effects[9] that arise from the nano size of the particles, which confine the movement of electrons.[1] Such properties generally allow them to improve the efficiency of

certain chemical reactions when acting as nanocatalysts, either by promoting faster reactions or by increasing the yield of product(s). Large surface areas are another special feature of these materials, where the fraction of atoms at the surface is greater than that of bulk compounds, providing a vast amount of space for chemical reactions to take place.[2,10] Furthermore, there are fewer neighbouring atoms at the surface; fewer neighbours decrease the binding energy of each atom, which affects their physical and chemical properties.[11]

The optical properties of nanoparticles, such as colour, are also noticeably different than their bulk counterparts.[12] For certain metal nanoparticles, in particular gold and silver, this is a result of a phenomenon known as surface plasmon resonance (SPR), which appears as a strong peak in the optical absorption spectra. SPR is described as a collective oscillation of surface electrons and is strongly dependent on the size and shape of the particle; due to the size of the particle being on the nanoscale, this process causes the strong difference in optical properties between nanoparticles and bulk materials.[13] Noble metal nanoparticles in particular have received considerable attention as nanocatalysts (such as Ru, Au, Pt, and Pd) due to their greater stability compared to other metals.[7,14,15] The property control of nanomaterials by fine-tuning their shape, size, and chemical stability allows for their applications in many fields such as electrocatalysis[16,17] and photocatalysis.[12,18]

1.2   Doping in Metal Oxide Nanoparticles

Metal oxide nanoparticles have received notable attention as photocatalytic alternatives to traditional wide bandgap semiconductors due to their unique optical properties.[18,19] They are resistant to oxidation at high temperatures because of their oxidized states and they exhibit

stability in a variety of chemical environments.[20] As with traditional semiconductors, doping

metal oxide nanoparticles can modify their atomic and electronic structure, allowing for control

over their physical and chemical properties through changes in the bandgap.[19] This

modification is done by introducing a dopant into the system (either non-metallic elements

such as nitrogen and carbon or transition metals).[20] Figure 1-1 shows a transition metal dopant

(tungsten) being introduced into the framework of titanium dioxide, wherein Ti vacancies and

dangling oxygen atoms are generated as a result. Some dangling oxygen atoms can escape and

generate oxygen vacancies in the lattice upon heating, resulting in the difference between the

initial and final structures, which consequently affects their catalytic properties.

The synthesis of doped metal oxide nanoparticles generally requires a wet-chemical

method, with two of the most popular being a hydrothermal method and a solvothermal

method.[18,20] Two widely used methods used to dope metal oxide nanoparticles are

coprecipitation and cohydrolysis of the parent metal precursor with either the dopant for metal

dopants or with a compound such as ammonia or urea for nonmetals.[19] A hydrothermal

synthesis uses high temperature and high-pressure water conditions to obtain nanoparticles

from precursors that are insoluble in more moderate conditions.[21] An electrostatic reaction

occurs between metal and hydroxyl ions to form the crystalline metal oxide nanoparticles at

temperatures typically less than 300 °C.[19] This technique allows for good control over the size,

composition, and shape of the nanoparticles, but the synthesis can be complicated by water

acting as both a stabilizing ligand and a solvent.[22] As such, solvothermal synthesis methods are

used in combination with organic solvents, which grant a better match in reactivity between

the metal oxide and dopant precursors while still allowing for good control over size and shape.[23]
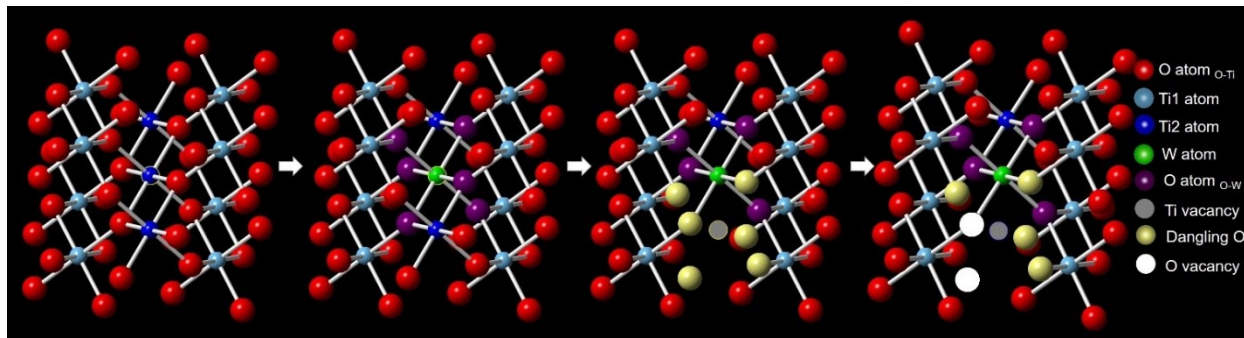
Figure 1-1: 3D models illustrating the introduction of tungsten atoms into a TiO_2 atomic structure.[24]

Zinc oxide and titanium dioxide are two of the most commonly used metal oxides for photocatalytic research due to their favourable properties compared to other metal oxides, such as their high stability and photosensitivity.[18,25] It has been reported that doping zinc oxide nanoparticles with magnesium causes a redshift in absorption and narrows the bandgap compared to pure zinc oxide, thus allowing their use in dye degradation.[26] Similar results can be observed for many other metal nanoparticles, in which doping can often enhance visible-light absorption by way of three main modes: a red shift of the bandgap to the visible region, an absorption tail extending into the visible wavelengths, and the introduction of new absorption peaks in the visible region.[19] In addition, doping can potentially reduce electron-hole recombination, as the dopant can cause spatial separation of electrons and holes through its interactions with the bulk material, which would prevent a decrease in photocatalytic activity.[27,28] As a result, doped metal oxide nanoparticles have seen a variety of photocatalytic applications such as oxygen evolution[29] and carbon dioxide reduction.[30]

4

1.3   Metal Nanoparticles on Zeolite Supports

Zeolites are aluminosilicate minerals that contain highly porous, uniform sites with large surface areas, permitting them to act as excellent supports for metal nanoparticles and preventing decreases in catalytic activity typically resulting from aggregation and sintering.[31–33] In addition to enhancing the stability of metal nanoparticles, zeolites can also increase their catalytic activities through a synergistic effect, in which they serve as an active support by acting as a co-catalyst.[34] Over 200 unique zeolite frameworks have been synthesized ever since Swedish mineralogist Axel F. Cronstedt first described their unique properties in 1756.[35]

Metal nanoparticles can be encapsulated inside of porous zeolites in one of two ways: introducing the metal nanoparticles into the already synthesized zeolite framework, or performing a one-step method in which the metal precursor and zeolite undergo co-crystallization and *in-situ* reduction.[33] For the purposes of this work, only the former method (called the wetness impregnation method) will be detailed. A soluble metal precursor is used to diffuse a metallic species into the crystal, loading into the pores of the zeolite after solvent removal (such as water or ammonia).[31] A reduction step is then performed to reduce the metal species into metal nanoparticles.[36] Figure 1-2 shows a diagram detailing the steps taken in the process of encapsulating the metal nanoparticles into a zeolite framework.
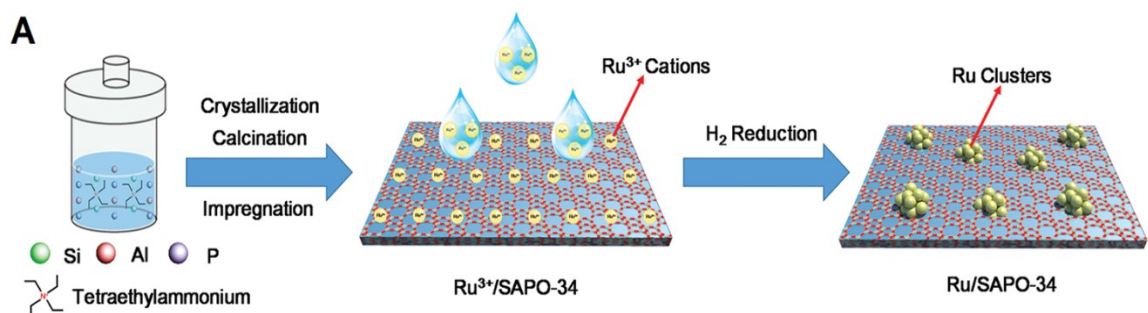
Figure 1-2: General synthesis procedure of depositing metal nanoparticles onto a zeolite support.[34]

The enhanced stability and greater catalytic activity provided by a zeolite support allows for the encapsulated metal nanoparticles to be used in a variety of catalytic applications.[37] Processes such as the catalytic oxidation of carbon monoxide can be performed with metal nanoparticles on zeolite supports, where the size of the metal nanoparticle can have an effect on the overall yield.[38] They also display high catalytic activity in both the dehydrogenation of alkanols and hydrogenation of alkenes.[32] As such, shape-selectivity and increased reaction rates can occur by avoiding using bulky substrates.[32]

1.4 General Outline and Motivations

Chapter 2 presents the experimental details of this work, wherein the theoretical background of X-ray absorption spectroscopy (XAS, the main technique used to probe information from nanoparticles) is provided. An in-depth look at the two main components of an XAS spectrum, the X-ray Absorption Near-Edge Structure (XANES) and the Extended X-ray Absorption Fine Structure (EXAFS), and a brief overview of some techniques used in XAS programs are provided.

Chapter 3 details the analysis of W-doped TiO_2 nanoparticles, nanomaterials that display excellent activity in the field of photothermal catalysis. Various doped samples of TiO_2 were examined using XAS, and greater understanding of the atomic structure was achieved using EXAFS fitting analysis.

Chapter 4 closely examines manganese cobalt oxides on carbon nanotube supports for their use as a catalyst in both the oxygen evolution and oxygen reduction reactions. XAS was used to study samples made with varying ratios of manganese and cobalt, which granted a deeper understanding of how the atomic structure of the nanocatalyst changed as the ratio of manganese to cobalt changed.

In Chapter 5, an examination of the effect of a bimetallic ruthenium-based nanoparticle system compared to a monometallic Ru system was performed, where such systems were supported on zeolites. Transmission electron microscopy techniques were used in addition to XAS to provide greater insight into the atomic structure of each sample.

Nanoparticles have seen much interest due to their unique properties, which allow them to be used in applications such as oxygen electrocatalysis. This work focuses on understanding their chemical and physical properties through in-depth structural analysis, which can prove vital in designing efficient, high-performance nanocatalysts for various catalytic applications. To this end, X-ray spectroscopy was used to study the atomic sites within a variety of metal nanoparticles.

Chapter 2: Experimental Techniques

2.1   Introduction to X-ray Absorption Spectroscopy

X-ray Absorption Spectroscopy (XAS) is a characterization technique that is useful in determining both the electronic properties and local bonding structure of various materials, among which are nanomaterials.[39] It is an element-specific technique, making it especially useful in the analysis of samples containing multiple elements, such as multiple-element alloys, as well as a non-destructive technique, allowing for further use of a sample in other characterization methods.[40,41] XAS is also an averaging technique, based on the atoms of the specific element being examined, which can provide information regarding the whole sample, unlike a characterization technique such as transmission electron microscopy, which only covers a small area of a sample.[40] Due to requiring high-energy X-rays, the technique is typically performed in synchrotron radiation facilities, resulting in measurements of high sensitivity.[40] Together with other characterization methods, such as X-ray photoelectron spectroscopy and powder X-ray diffraction, XAS can provide greater understanding of the electronic and structural properties of nanomaterials.

XAS experiments obtain the absorption spectrum of a single chemical element by way of exposing a sample (typically a metal foil or compacted powder on a surface that will not influence absorption readings, such as Kapton tape) to a beam of X-rays, where the energy of the X-ray beams is continuously modified. When X-ray beams of sufficient energy are reached that can excite a core electron within the sample to a higher, unoccupied state, the core electrons are promoted to higher energy states, resulting in the absorption measurement

dramatically increasing and giving rise to a sharp, rising edge in the spectrum, referred to as the absorption edge.[41] At the absorption edge, the X-ray energy needed to excite a core electron is equivalent to that of the electron binding energy, and due to such binding energies being element-specific, it results in XAS also being an element-specific characterization technique.[42] The transition between the initial and final state determines the type of edge under study – the most commonly studied edges being the K-edge and the L_{III}-edge, which involve a 1s electron transitioning to a valence p state, the p state depending on the element examined (a Pd K-edge studies the 1s to 5p transition), and a 2p electron to valence d-state (such as the Au L_{III}-edge being a 2p to 5d transition), respectively.[41] Such transitions are determined by dipole election rules, in which:

$$\Delta l = \pm 1 \tag{1}$$

In equation (1), Δl represents the difference of the final and initial electronic state angular momentum quantum numbers. A list of absorption edges and their respective electronic transitions can be seen in Table 2-1.

Table 2-1: The most common absorption edges and their corresponding electronic state transitions observed in XAS.

Absorption Edge	Initial State	Final State
K	1s	p
L_I	2s	p
L_{II}	$2p_{1/2}$	s, d
L_{III}	$2p_{3/2}$	s, d
M_I	3s	p
M_{II}	$3p_{1/2}$	s, d
M_{III}	$3p_{3/2}$	s, d

An X-ray beam passing through a sample typically experiences a loss in intensity, which is described by μ, the X-ray absorption coefficient. μ can be determined by the following equation:

$$\mu(E) = \log\left(\frac{I_0}{I}\right) \tag{2}$$

I_0 and I represent the intensity of the X-ray beam before and after it is incident on the sample, respectively. The X-ray absorption coefficient μ is strongly influenced by the local environment of the atom being studied, reflected in the oscillations that can be observed in a typical X-ray absorption spectrum.[40,41]

Continuous exposure to an increasing amount of X-ray energy results in a core electron becoming a "free electron" in an unbound state known as the continuum, due to being able to overcome the binding energy. This results in the absorbance measurements after the absorption edge to give absorbance readings far above the initial ground state absorbance. The XAS spectrum obtained from a synchrotron experiment can be separated into two main components: the X-ray Absorption Near-Edge Structure (XANES), which encompasses the pre-edge, absorption edge, and a small amount of the post-edge region, and the Extended X-ray Absorption Fine Structure (EXAFS), composed of a majority of the post-edge region (Figure 2-1).
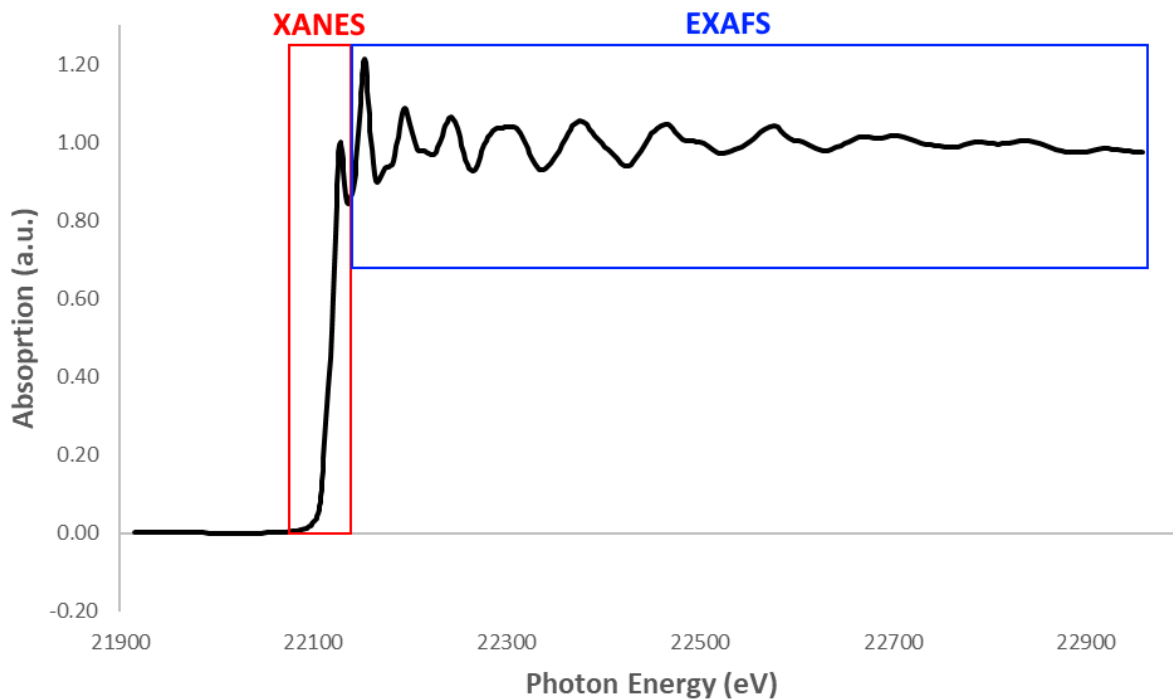
Figure 2-1: Normalized XAS Spectra of ruthenium foil, measured at the Ru K-edge. XANES and EXAFS regions of the spectra have been identified.

2.2   X-ray Absorption Near-Edge Structure (XANES)

The XANES region of an XAS spectrum is comprised of the pre-edge and absorption edge regions, as stated above. Typically, this region encompasses a range of approximately 40 eV behind and past the absorption edge.[40,41] The XANES region can give information regarding the electronic properties of the sample under study.[43] The XANES pre-edge region can sometimes exhibit what are known as "pre-edge features", which come about as a result of electronic transitions that are lower in energy than the excitation energy of the core electron (the absorption edge energy).[44] At the absorption edge region, commonly referred to as the "white line", electronic transitions of the core electron to unoccupied states allow for information of the oxidation state to be obtained. By measuring multiple references with known oxidation

states, one can compare them to an unknown sample and be able to roughly determine the oxidation state of the element. Higher oxidation state elements exhibit greater intensity white lines, due to a greater amount of unoccupied states being present.[45] Furthermore, the edge shift compared to the known metal foil (each element has a characteristic edge shift; for example, ruthenium foil has a characteristic edge energy of 22117 eV) can also provide information on the oxidation state: positive charge shifts the edge to a higher energy, whereas a negative charge shifts the edge to a lower energy.[46] It should be noted, however, that the edge shift is far more accurate for low energy XANES.[40,41]

Multiple scattering photoelectric effects also provide information that can be observed in the XANES region. Photoelectrons created as a result of the excitation of the core electron can travel in multiple directions, in which they can be scattered off of multiple atoms before returning to the original absorbing atom.[47] Due to the large number of possible scattering paths that photoelectrons can take, the oscillations that immediately follow the absorption edge are produced as a result (Figure 2-2).[48] These scattering paths can provide information concerning the structure around the absorbing atom, including the lattice type of the metal system.[41]
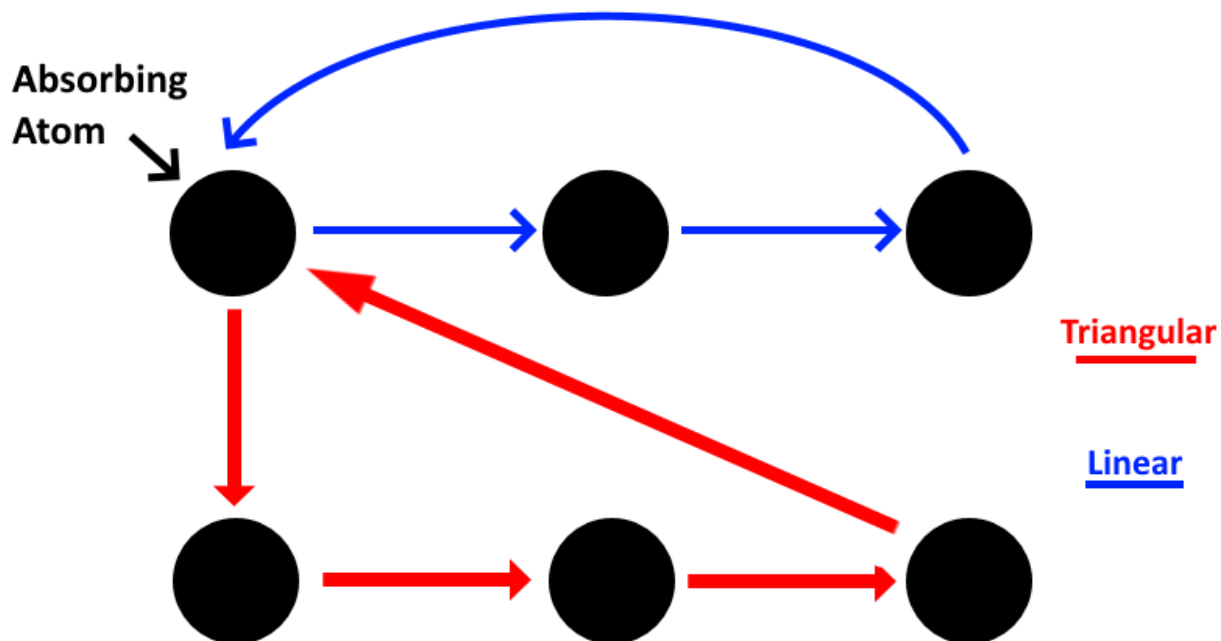
Figure 2-2: Diagram detailing multiple scattering paths, showing a triangular and linear multiple scattering path. Various multiple scattering paths are possible.

2.3   Linear Combination (LC) XANES Fitting

LC XANES fitting, used in the WinXAS fitting program[49], provides a simulation of an experimental XANES spectrum by a linear combination of known reference samples. Used in analysis of multi-component samples, it can quantify each component in the samples from the near-edge region by comparing their normalized XANES spectra with linear combination results of known references.[50] A least-squares procedure is used in the algorithm to refine the sum of a given number of reference spectra to an experimental spectrum (Figure 2-3). Two parameters – c, partial concentration, which is the determined percentage of the particular component and E, energy correction, which corrects for differences in energy calibration, are determined (Figure 2-4).
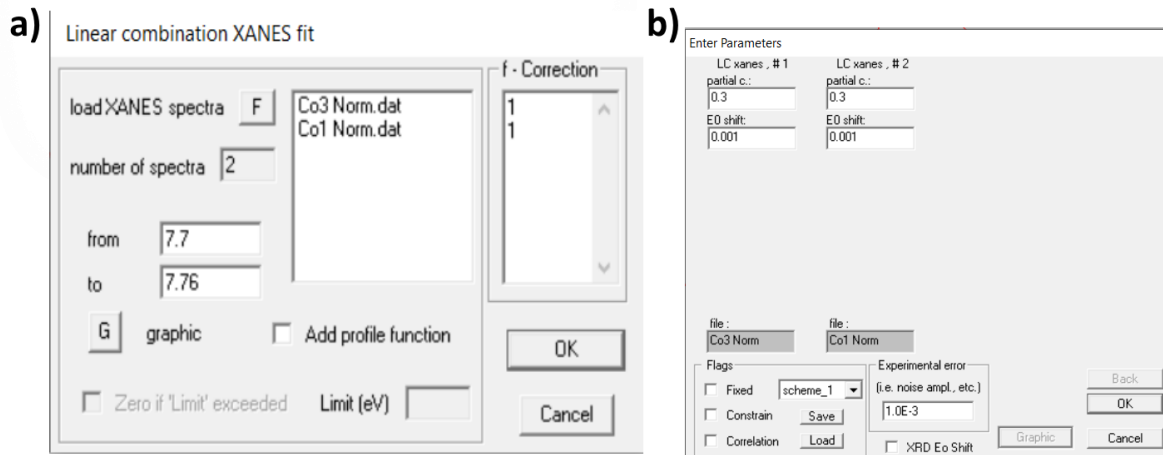
Figure 2-3: WinXAS LC XANES fitting operation windows. In the first step a) one inputs known references into the program to be compared to the unknown (Co3 Norm: Co_3O_4 and Co1 Norm: Mn_2CoO_4 in the example) as well as the range for which the fit is performed, and then b) guess parameters are used to approximate the values.
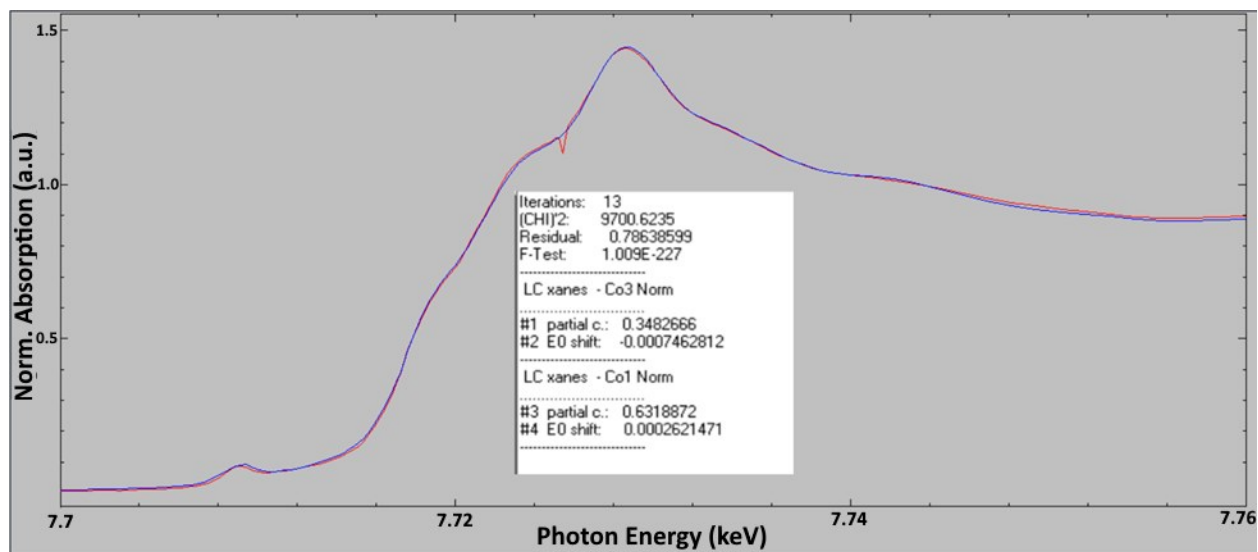
Figure 2-4: WinXAS window showing a completed LC XANES fit.

2.4 Extended X-ray Absorption Fine Structure (EXAFS)

The EXAFS region is largely encompassed by the region 40 eV after the absorption edge, where small oscillations are typically observed. As stated before, an excited core electron promoted to the continuum becomes a free electron, or a photoelectron wave. The photoelectron wave travels through the sample until it reaches a neighbouring atom, at which point the electron density of the neighbouring atom backscatters the photoelectron wave back to the original absorbing atom (Figure 2-5).[51] The phase and amplitude of the backscattered photoelectron is dependant on both the energy of the photon and the neighbouring atom element.[40,41] Constructive or destructive interference will then occur between the backscattered wave and the original photoelectron wave. The absorption coefficient will increase or decrease if the two waves are in phase and out of phase, respectively.
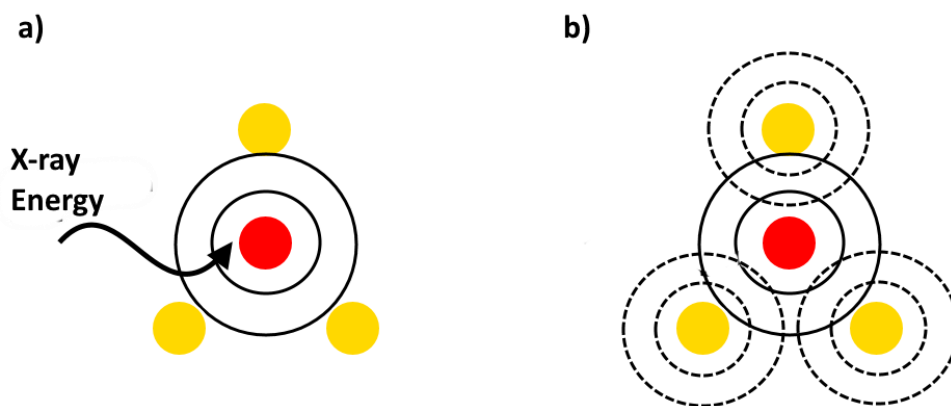
Figure 2-5: Schematic depiction of photoelectron scattering, which causes changes in the absorption coefficient. It involves a) absorption of X-ray energy, which is then ejected as a photoelectron wave, and b) backscattering of the photoelectron wave off of neighbouring atoms.

Using the measured absorption coefficient μ, one can obtain the fine structure χ through the

equation:

$$\chi(E) = \frac{\mu(E) - \mu_0(E)}{\Delta\mu_0(E)}$$ (3)

In the equation above, μ_0 is a background function that measures the absorption of an isolated

atom, typically contrasting the oscillations seen in a typical EXAFS region by being smooth, and

$\Delta\mu_0$ is the change in the absorption coefficient before and after the absorption edge. However,

EXAFS is best understood in terms of the wave behaviour of the photoelectron created. As

such, χ is commonly depicted as function of k, the photoelectron wavenumber, which can be

converted from the X-ray energy, defined as the following:

$$k = \sqrt{\frac{2m(E - E_0)}{\hbar}}$$ (4)

In the above equation, m is the electron mass (9.109×10^{-31} kg), E is the energy of the incident

photon, E_0 is the binding energy of the core level electron (equivalent to that of the absorption

edge energy), and $\hbar$ is the reduced Planck constant. The resulting spectrum is commonly

referred to as a k-space. $\chi(k)$ is multiplied by k^n to account for the dependence of the

backscattering amplitude on the energy and atomic number of the neighbouring atom, where n

is 0, 1, 2, or 3, and as such the resulting spectrum is said to have a k-weighting of n. The

spectrum can then be subjected to a Fourier transform to isolate certain signals based on

distance from the absorbing atom, giving what is called an R-space, which can provide

structural information of the local bonding environment around the absorbing atom (Figure 2-

6).
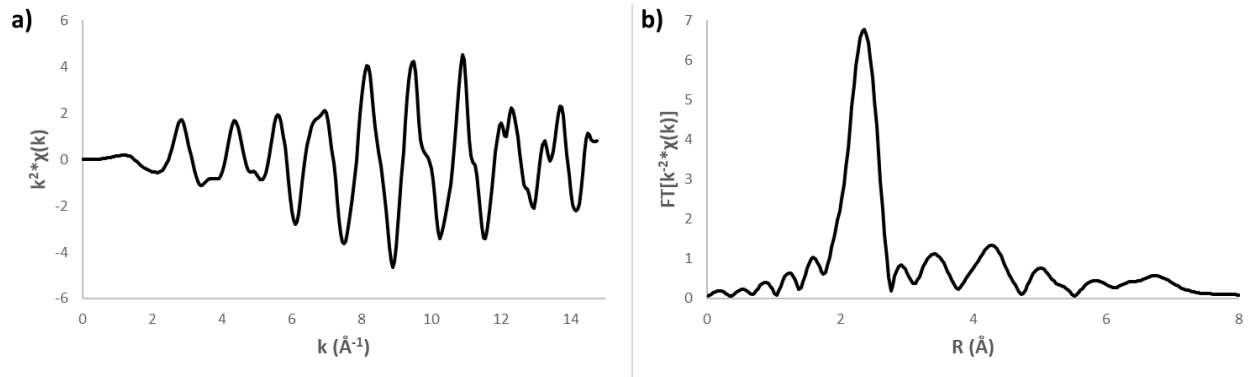
Figure 2-6: a) K-space of ruthenium foil with a k-weighting of 2 and b) Fourier transformed k-space, where intense peaks represent pseudo radial bond distribution about the absorbing Ru atom; here, the intense peak is indicative of the first Ru-Ru coordination shell at 2.65 Å.

Both the peak position and peak intensity can be used in qualitative analysis; the position of the peak can indicate if the neighbouring atom is a metal or non-metal, and the intensity is typically proportional to the coordination number.[40] The bond distance of the neighbouring atom to the absorbing atom, however, cannot be determined without proper fitting procedure due to phase shifting.[52]

The EXAFS equation is used to physically describe the bonding environment of the absorbing atom:

$$\chi(k) = \sum_j \frac{S_0^2 N j}{kR^2} e^{-\frac{2R}{\gamma(k)}} e^{-2\sigma^2 k^2} f(k) \sin[2kR + \delta(k)] \tag{5}$$

The EXAFS equation has *f(k)* and *δ(k)* represent the scattering properties of neighbouring atoms, the backscattering amplitude and phase shift, respectively, *k*, the wavenumber of photoelectrons, *N*, the coordination number, *R*, the distance from the absorbing atom to the neighbouring atom, σ^2, the disorder in the neighbour distance (Debye-Waller Factor), S_0^2 and γ

17

as the amplitude reduction factor and mean free path, respectively, which account for losses of coherence of the photoelectron, and j, which accounts for different scattering paths. By using an EXAFS fitting program, such as WinXAS or Artemis[53], the EXAFS equation can be solved for N, R, and σ^2, if both the scattering amplitude f(k) and the phase shift $\delta(k)$ are known, typically by referring to reference spectra of known compounds.

Using Equations 3, 4, 5, and 6 can be vastly simplified by means of an EXAFS fitting program. A general fitting procedure using the EXAFS fitting program WinXAS for a palladium foil (a metal with a face-centered cubic crystal structure) is described herein. The raw data obtained from a synchrotron experiment is first normalized using Equation 3. In the WinXAS program, this is performed through a two-polynomial fit background correction, seen in Figure 2-7.
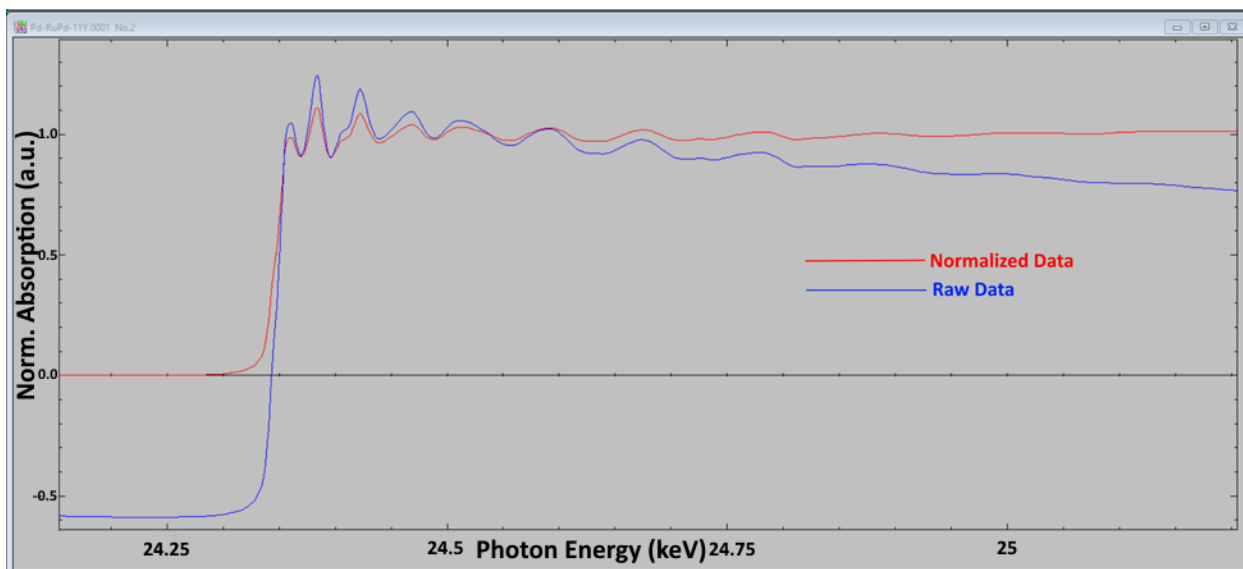
Figure 2-7: WinXAS data graph displaying both the raw data and normalized data of a Pd metal foil sample.

The data is then converted to a *k*-space through Equation 4. In the WinXAS program, this is done through setting the normalized data's E_0 (at the absorption edge of the element and studied) and processed through a mue(0)-fit. A converted data spectrum can be seen in Figure 2-8.
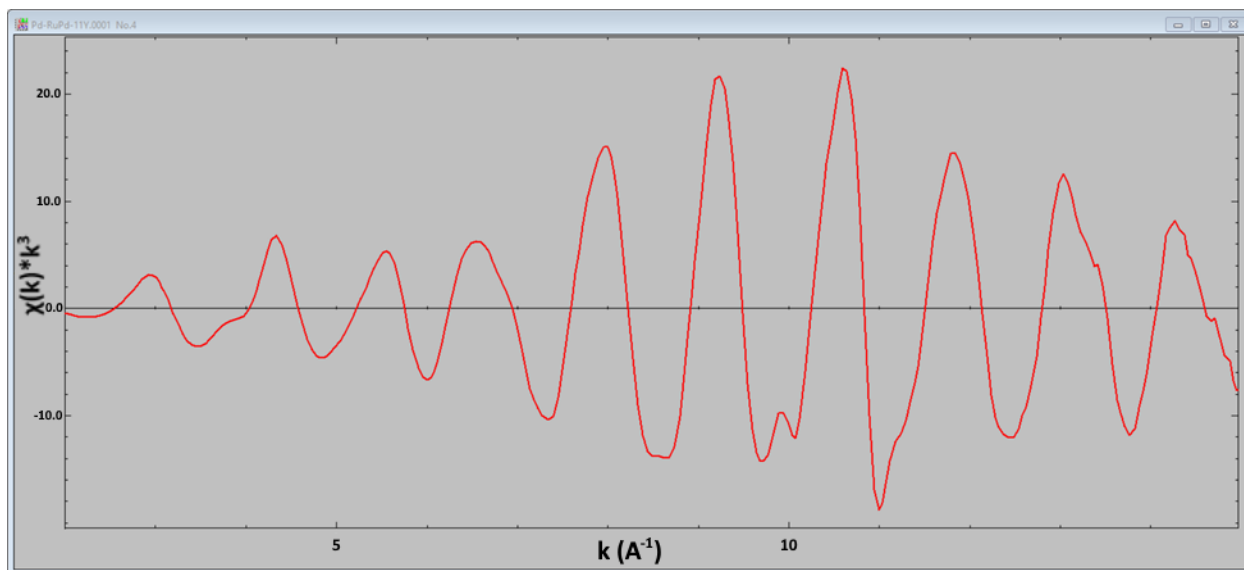
Figure 2-8: *k*-space of Pd metal foil with a *k³* weighting.

As described in Figure 2-6, the *k*-space data is then made to undergo a Fourier Transformation. For a reference metal foil, the quality of both the *k*-space and Fourier Transformed data is expected to be high. Solving for N, R, and σ^2, as described in Equation 5, is performed through EXAFS refinement fitting. Using a FEFF input file, which is generated through a program known as FEFF8[54], allows for fitting of data based on approximations made in the FEFF8 program, where one provides data of a crystal structure that best represents the data. In this case, because the sample being measured is a known metal foil, the palladium-palladium bond length of 2.75 Å can be used in the input file for fitting, as seen in Figure 2-9.
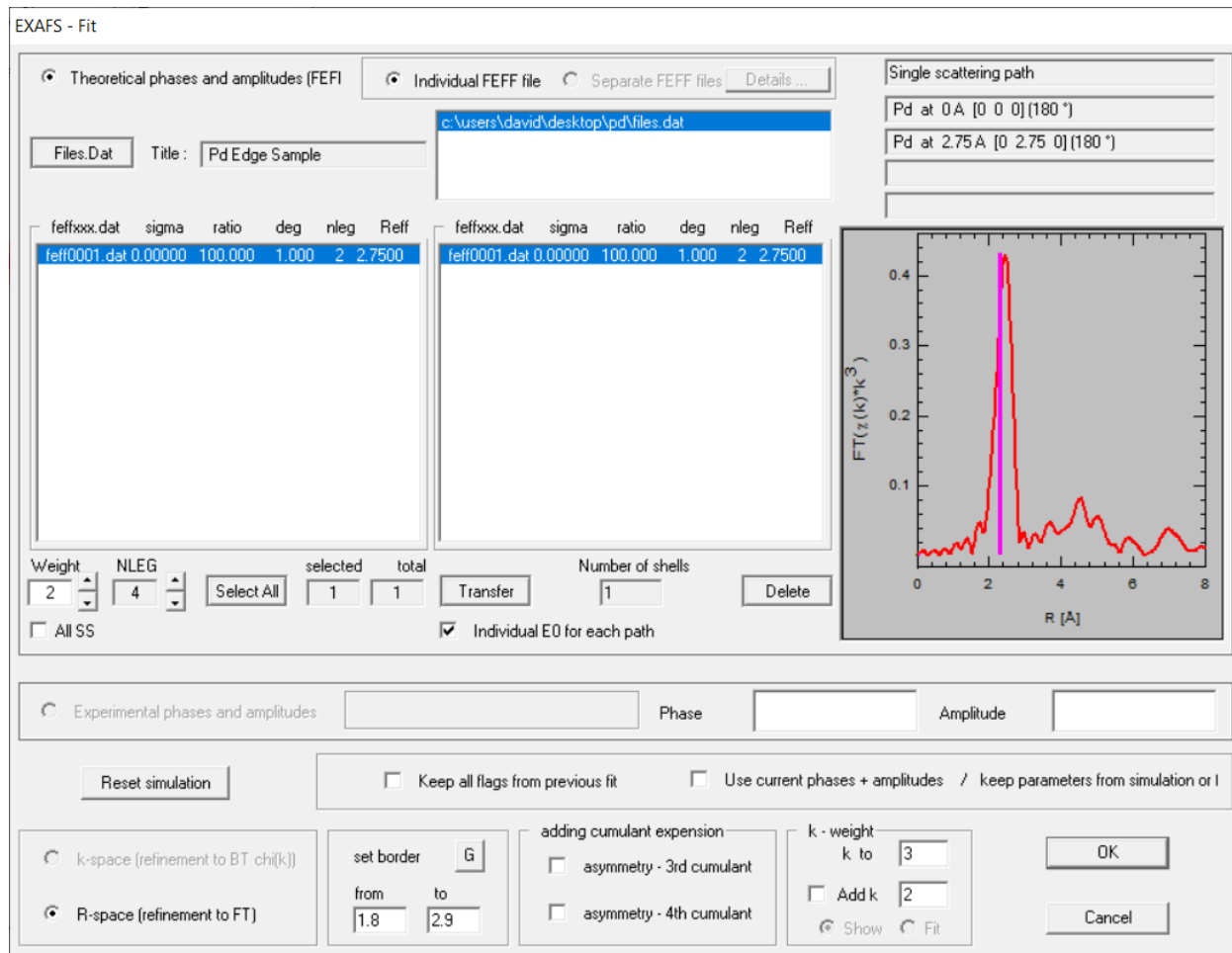
Figure 2-9: WinXAS EXAFS fitting window, where parameters for fitting are inputted. The R-window (the range for which the fitting is performed) and the bonds fitted are both determined.

The fitting results are then obtained, and one can determine the quality of the fit both qualitatively (seeing how well the fit matches the experimental data) and quantitively (comparing the fitting results with data found in literature). In Figure 2-10, the fittings results of Pd metal foil can be seen. One can see that the coordination number, at 11.24, is incredibly close to that of a bulk Pd, which is known to have a coordination number of 12.[55] The bond

distance of the Pd-Pd bond, 2.74 Å[55], is also, within uncertainty, equal to that of bulk Pd. For

unknown samples, it is likely that many more bonds are present (such as through oxidation or

being a multiple-element sample), and as such, the fitting process becomes more complicated.

Due to the number of variables being greater with more bonds, it is possible for the number of

guess variables to exceed that of the available information content of the data of the R-

window. In such as case, the E_0 and σ^2 variables of each bond can be correlated to reduce the

number of guess parameters.
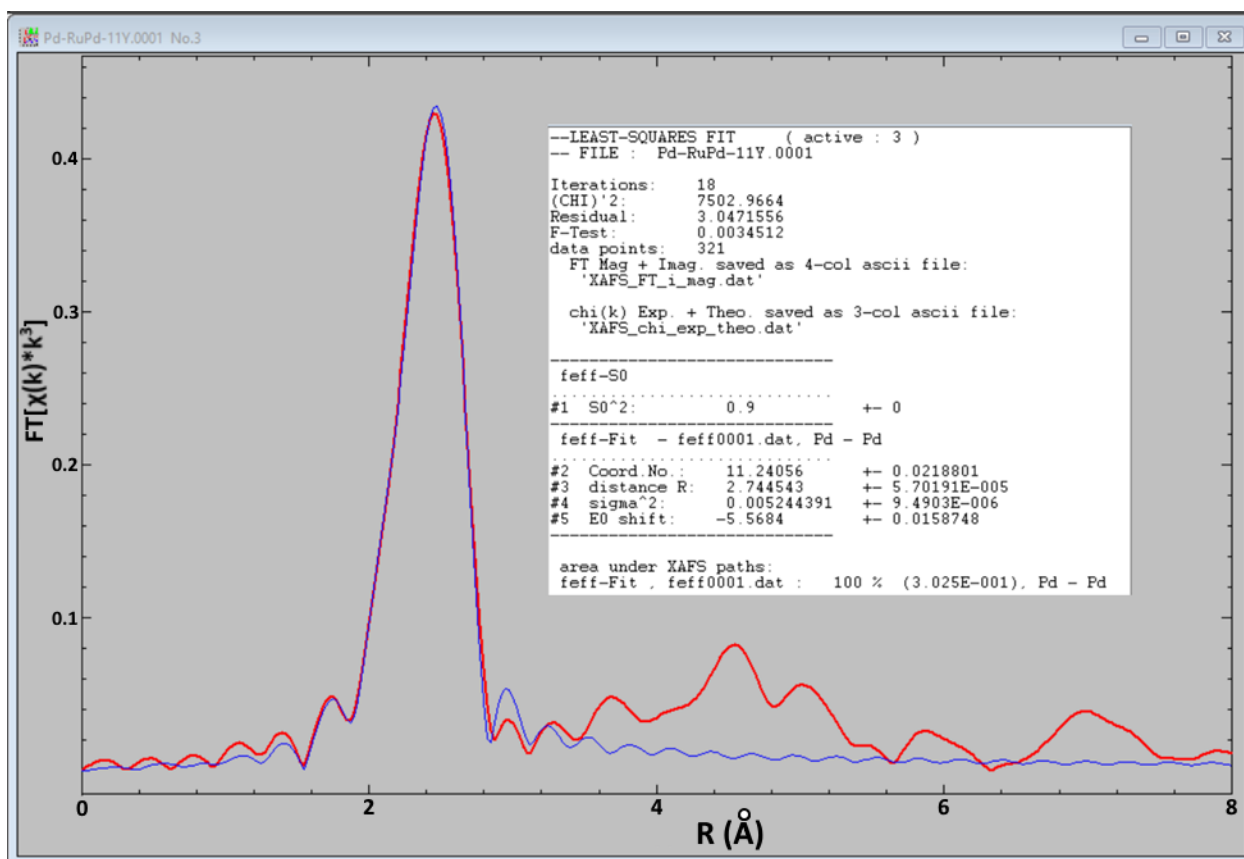
Figure 2-10: Fitting Results of Pd metal foil using the WinXAS program. The blue line is the

simulated fit, whereas the red line is the experimental Fourier Transformed data.

Chapter 3: X-ray Absorption Spectroscopy Analysis of W-Doped TiO$_2$

Nanoparticles

Part of the results in this chapter was reproduced with permission by the RSC from Li, Y.; Walsh, A. G.; Li, D.; Do, D.; Ma, H.; Wang, C.; Zhang, P.; Zhang, X. W-Doped TiO 2 for Photothermocatalytic CO 2 Reduction. *Nanoscale* **2020**, 17245

Contrubutions: David Do performed the XAS data extraction, fitting analysis and analyzed the XAS results. All other experimental work was conducted by Yingying Li (Northeast Normal University, China).

3.1   Introduction

TiO$_2$ is a widely studied catalyst that has displayed excellent activity in the field of photothermal catalysis. As such, various methods to alter the structure of TiO$_2$ have been reported in literature, in order to determine the possibility of enhancing its catalytic activity.[56–58] Doping the material with foreign atoms has been performed as one such method, with the intention of generating defects within the lattice of TiO$_2$. Defects in the TiO$_2$ lattice are considered to be efficient catalytic sites for photothermalcatalysis, in particular the absorption of CO$_2$ during the process of photothermocatalytic CO$_2$ reduction.[59] Tungsten has received significant attention as a dopant for TiO$_2$ due to the radius of W^{6+} being similar to that of Ti^{4+}, which reduces the change in the crystal structure of the doped material, while also allowing for noticeable changes in the catalytic properties.[60,61]

The electronic structure and bonding properties of these W-doped TiO$_2$ nanocatalysts are of significant interest, as they can provide a greater understanding of the mechanism by which CO$_2$ reduction is performed, as well as insight on the effect of the concentration of dopant introduced into the lattice. XAS (on the titanium K-edge and tungsten L$_{III}$-edge) is a

powerful characterization technique that can analyze the changes, if any, in titanium-bonding and the presence of tungsten bonding within the lattice of the doped samples. Additional characterization techniques, such as scanning electron microscopy (SEM) and X-ray powder diffraction (XRD), can further support findings from XAS, and allow for a clear image of the crystal structure of the doped TiO_2 samples.

3.2   Experimental Methods

3.2.1   Synthesis of W-Doped TiO_2 Samples

The synthesis of the one-dimensional rutile TiO_2 nanostructures was performed and detailed in previous work[62], as was the procedure in which the TiO_2 samples were doped with tungsten.[24] A brief summary of the synthesis of W-doped TiO_2, important to this writing, is provided. A mixture of 2 g P25 TiO_2 powder, 8 g NaCL, and 2 g $Na_2HPO_4 \cdot 12H_2O$ was ground for 30 minutes, and was then calcinated at 825 °C for 8 hours. Following that, impurities were removed from the system by boiling the mixture in deionized water and was then dried at 110 °C for 24 hours. $(NH_4)_{10}W_{12}O_{41} \cdot {\sim}XH_2O$ was then added to four different samples of 4 grams of TiO_2, with molar ratios of W/Ti used being 0%, 2%, 4%, and 10% (herein referred to as TW0, TW2, TW4, and TW10, respectively). Finally, the samples were calcined at 750 °C for 30 seconds in a rapid-annealing furnace.

3.2.2   X-ray Absorption Spectroscopy

XAS measurements were conducted and obtained using the Sector 9-BM and Sector 20-BM beamlines at the Advanced Photon Source (APS) at Argonne National Laboratory (Argonne National Laboratory, IL). Powder samples were measured by packing powder in washers

23

supported and sealed on Kapton tape for the purpose of adequate X-ray absorption. Tungsten

measurements were taken in fluorescence mode, with the exception of the $(NH_4)_{10}W_{12}O_{41}$

reference, which was taken in transmission mode alongside the titanium measurements. At

least five scans were performed for each sample, under ambient conditions at room

temperature.

3.2.3   XAS Data Analysis

XAS data processing and fitting for the W-doped TiO_2 samples was performed with data

processing programs Athena and Artemis.[53] As $(NH_4)_{10}W_{12}O_{41}$ is a known reference, its

crystallographic data was used to determine the amplitude reduction factor, S_0^2, as 0.72, by

fixing known coordination number (CN) values. For the Ti K-edge samples, the S_0^2 was obtained

from fittings of all four samples with no fixed parameters, resulting in values ranging from 0.14 –

0.17; an average of 0.16 was deemed to be reasonable. All samples had a k-weighting of 2. A k-

range of 3.0 – 10.4 $Å^{-1}$ and 3.0 – 11 $Å^{-1}$ was used for the W L_{III}-edge and Ti K-edge, respectively.

An R-range of 0.9 – 2.35 Å and 1 – 2 Å were also respectively used for the refinement of the W

L_{III}-edge and Ti K-edge. For the W L_{III}-edge, the Debye-Waller (σ^2) and E_0 shift values were

correlated for samples having two tungsten-oxygen shells in order to reduce the number of free

running parameters.

3.2.4   Other Characterization Techniques

XRD patterns were collected on a Rigaku, D/MAX 2500 X-ray diffractometer with Cu Kα

radiation, all samples being measured on a quartz substrate. SEM images were obtained on a

Quanta 250 FEG with accelerating voltage 30.00kV to obtain morphology information of the

samples. Photothermal CO_2 reduction was also measured in an autoclave of 100 mL. The

system contained 0.05 g powder and 2 mL deionized water, and was then sealed and blown with

99.999% CO_2 for 20 minutes to ensure a pure carbon dioxide atmosphere within the system.

The system was irradiated with a 150 W UV Hayashi UV410 lamp, with a light intensity of 20

mW/cm^2 at a wavelength of 365 nm (determined by a light intensity meter). The temperature

was monitored with a thermocouple and was controlled at 393 K. CO generation was

monitored using a gas chromatograph (GC-2014, Shimadzu Co., Ltd.), and photothermocatalytic

activity was tested twice for each sample.

3.3   Results and Discussion

3.3.1   Non-XAS Characterization Method Results

As can be seen in the SEM images displayed in Figure 3-1a, all W-doped TiO_2 samples

exhibited one-dimensional nanostructure features that could be described as nanorods or

nanowires. The length of each sample was determined to be mainly between 0.6 μm and 2.0

μm, and the diameter of each sample was within the range of 60 nm and 120 nm. No

significant morphological change was observed upon the introduction of tungsten into the TiO_2,

nor was any obvious aggregation of tungsten on the surface of the TiO_2 reflected in elemental

mapping images.

All four samples analyzed showed the same main XRD peaks (shown in Figure 3-1b),

which are characteristic of the rutile phase of TiO_2.[63] Such results are an indication of tungsten

doping not causing any significant difference in the TiO_2 lattice structure; the lattice is

maintained. Increasing the W concentration to 10% allows for the observation of new low-

intensity peaks at 22.7°, 24.0°, 28.2°, 33.1°, and 34.0°, which can be seen in Figure 3-1c. These

peaks can be attributed to WO_3, which indicates that, when the tungsten dopant concentration

is at 10%, small amounts of WO_3 are formed. The same peaks are also visible in TW4, but are

much less intense, being barely visible. As such, the 4% doping represents a maximum

concentration for the bulk lattice doping of TiO_2; further increases in tungsten concentration

result in the formation of WO_3 outside of the TiO_2 lattice.
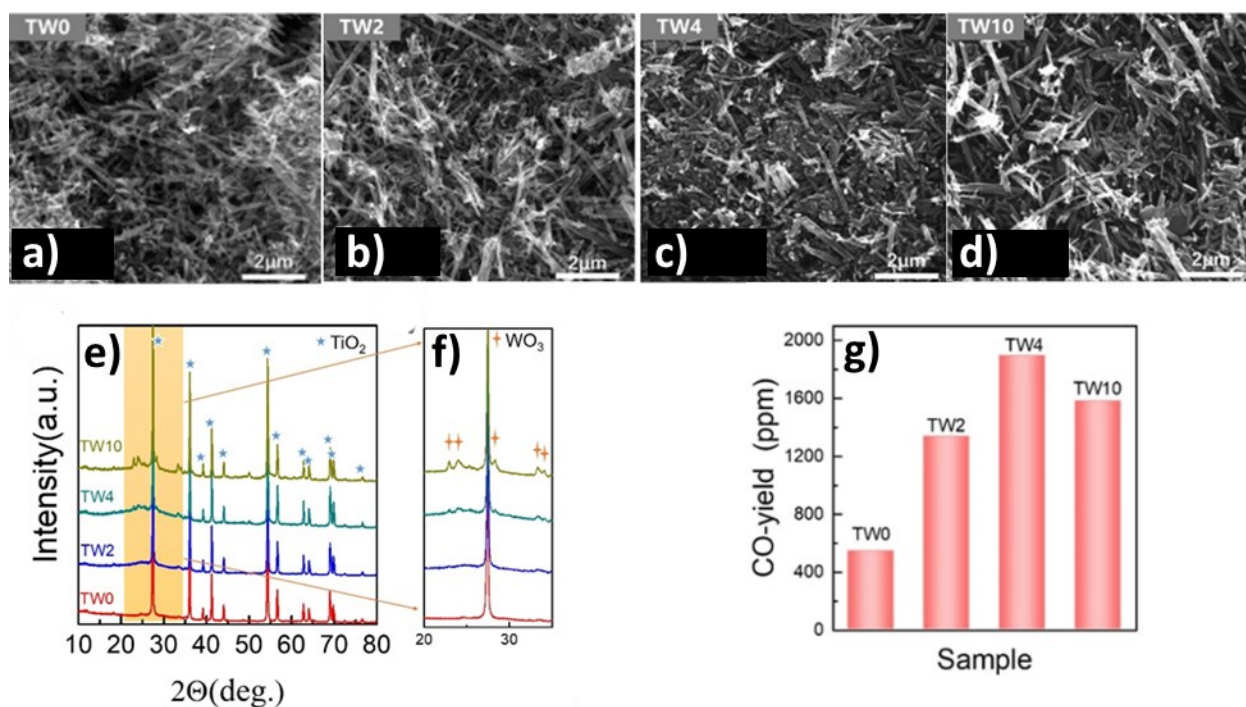
Figure 3-1: SEM images of (a) TW0 (upper left), (b) TW2 (upper right), (c) TW4 (lower left), and

(d) TW10 (lower right), (e) XRD patterns and (f) magnified XRD patterns of samples in region of

20° - 35°, and (g) Photothermalcatalytic induced CO_2 Conversion over TW0, TW2, TW4, and

TW10

The photothermocatalytic performance of the four samples were examined by measuring CO_2 reduction under UV light at a constant temperature. Results are shown in Figure 3-1d. The W-doped samples showed significant improvement over the undoped sample with respect to CO-production. In particular, TW4 produced 3.5 times more CO than TW0. Noticeably, the CO-yield for TW10 (roughly 1600 ppm) is less than that of the CO-yield of TW4 (about 1900 ppm), which is inconsistent with the trend set by TW0, TW2, and TW4, where one would expect that the CO-yield would increase as the tungsten dopant concentration increased. This is consistent with the XRD results, in which the formation of WO_3 is observed as the tungsten concentration is increased beyond 4%. Further analysis on the correlation between these two findings is done later in this writing.

3.3.2 XAS Analysis of W L_{III}-edge

XAS measurements were conducted to obtain more information on the atomic structure and electronic properties of W and Ti in the W-doped catalysts. Figure 3-2 shows the XANES spectra, in which it can be seen that all four samples exhibited similar peak shapes to one another, which is an indication of them sharing similar electronic properties.[41] The W reference sample, $(NH_4)_{10}W_{12}O_{41}$, had the least intense white line amongst the four samples, which is indicative of the sample having the highest d electron density.[64] In addition, the white line intensity increased as the W doping content decreased; the next most intense white line came from the TW10 sample, followed by the TW4 sample, with TW2 having the most intense white line. A clear downward trend with respect to d electron density is seen as the amount of doped tungsten decreased within the samples measured. A low d electron density corresponds to a greater positive charge of the element being measured.[45] Therefore, this result indicates that

27

TW2 has the highest tungsten positive charge, followed by TW4, with TW10 having the lowest tungsten positive charge of the three doped samples, and the tungsten reference compound has the lowest W positive charge amongst all the samples. The overall oxidation state of tungsten is not significantly affected, however, as the observed variations in positive charge are all relative to the tungsten reference compound.
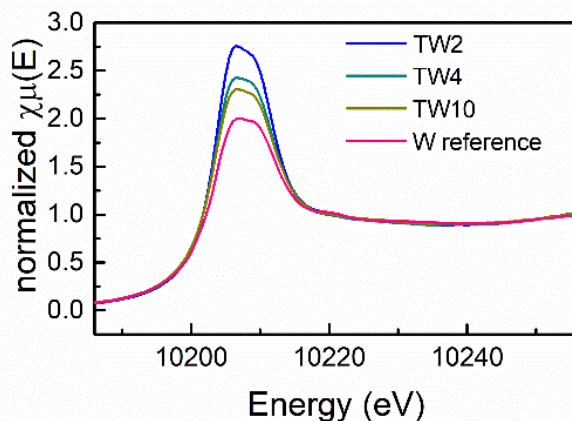
Figure 3-2: W L_{III}-edge XANES Spectra of TW2, TW4, TW10, and reference $(NH_4)_{10}W_{12}O_{41}$ Samples

EXAFS measurements were performed in order to obtain details on the local structure of the three doped samples with respect to the W-reference. The Fourier-Transformed EXAFS (FT-EXAFS) spectra and their best fits are provided in Figure 3-3. Each FT-EXAFS spectrum showed an intense peak in the region between 1-2 Å, which corresponds to interactions between metal and non-metal atoms; in this case, the interactions are between tungsten and oxygen. The W-reference CNs for the fitting results shown in Table 3-1 were obtained through analysis of the crystal structure of the compound. An upward trend within the first tungsten-oxygen shell CN of the doped samples is observed as the amount of dopant is decreased.
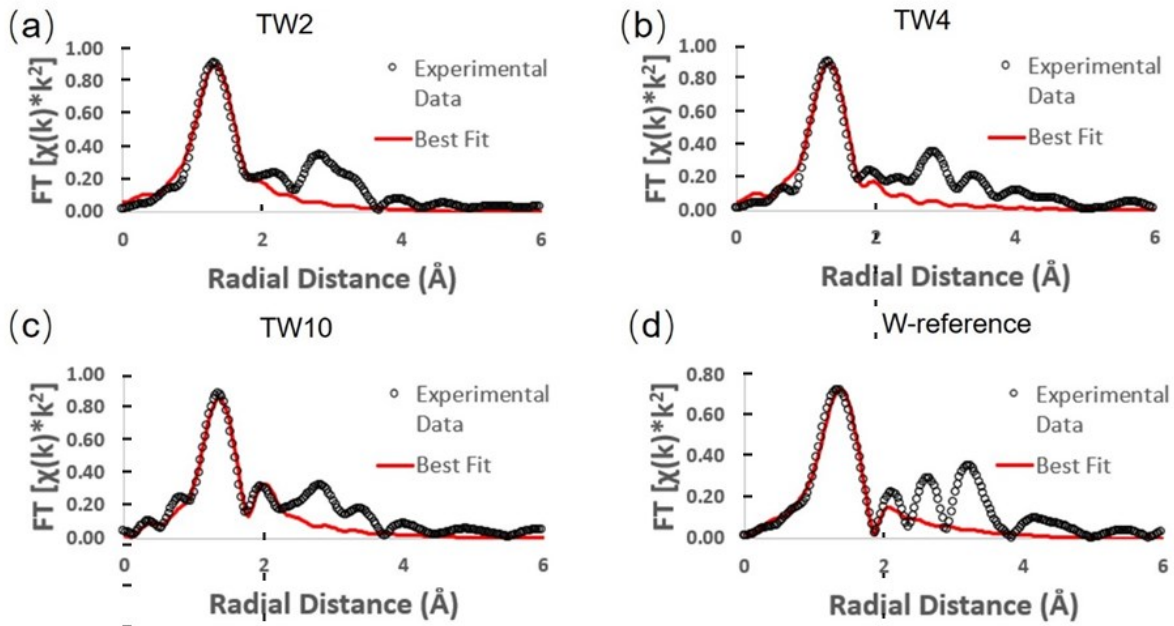
Figure 3-3: W L_{III}-edge FT-EXAFS Spectra of TW2, TW4, TW10, and reference $(NH_4)_{10}W_{12}O_{41}$ Samples

In order to understand these EXAFS fitting results, the unit cell structure of TiO_2 and the W-reference must be considered. The TiO_2 unit cell is essentially an octahedron structure containing one titanium atom bonded to six oxygen atoms. The six Ti-O bonds can be divided into two groups, four of them having a bond distance of 1.965 Å and the other two having a bond distance of 1.984 Å. The difference in bond distance between these groups of bonds, however, is very small (0.019 Å) and thus these six metal-oxygen bonds can be considered as one shell in the EXAFS fitting. The W-reference compound also has an octahedron structure; it has four of the tungsten-oxygen bonds at 1.852 Å and the other two at 2.242 Å, known values from averaging the crystallographic data. Compared with TiO_2, these two groups of W-O bonds show a large difference in bond distance (0.39 Å) and therefore must be fitted with two shells in EXAFS fitting procedures.

29

Table 3-1: W L_{III}-edge EXAFS Fitting Results of W-doped TiO_2 Samples Scanned in Fluorescence Mode

Sample	Shell	CN^a	R (Å)	σ^2	E_0	R-Factor
TW2	W-O	4.8 (9)	1.78 (2)	0.009 (3)	3 (3)	0.020
TW4	W-O	3.6 (9)	1.78 (2)	0.006 (3)	3 (3)	0.022
TW10	W-O	3.1 (9)	1.80 (2)	0.005 (4)	9 (3)	0.012
		1.2 (7)	2.36 (7)			
W-reference	W-O	4.33	1.81 (3)	0.011 (7)	12 (6)	0.019
		1.67	2.22 (5)	0.009 (8)		

^{a}Coordination Number. Reference compound values fixed from crystallographic data.

The fitting results show that the trend of CNs over the three doped samples is consistent with the results determined from XANES. The higher positive charge of the W-doped catalysts as observed in Figure 3-3 can be attributed to electronegative oxygen atoms withdrawing electrons from tungsten. A higher CN of the shortest bond distance W-O shell (i.e. more O atoms bonded to W) would result in more electron transfer from tungsten to oxygen, leading to a more positive charge on tungsten. Notably, the CN for the W-O shell of TW2 is close to 5, which is near that of a standard titanium atom in the TiO_2 unit cell (CN = 6). Tungsten atoms inside the TiO_2 lattice replaced titanium atoms, which increased the W-O CN with respect to W-reference. To keep the neutral charge of semiconductor after doping W of higher valence (6+), some vacancies of the Ti atom (4+) will appear. Another possibility is to form lower valent Ti species in the sample.

When the tungsten concentration increases from 2% to 4%, the amount of Ti vacancies should also increase to keep the charge neutrality of the semiconductor. Consequently, the amount of dangling oxygen atoms increased and more oxygen atoms became unstable. Since the valence of W is higher than that of Ti, the Ti vacancies should be mainly formed in the nearest shell around the W centre.

As seen in Table 3-1, the CN of the W-O shell in TW2 is higher than TW4, which indicates that oxygen vacancies were produced around the tungsten centre when the dopant concentration increased from 2% to 4%. The difference in W-O shell CN is can be attributed to the increased Ti vacancies. The dangling oxygen atoms between W and Ti vacancies tended to be unstable and easily escaped from the lattice during heating in the synthesis. This also means that the amount of oxygen vacancies and dangling oxygen atoms were increased from 2% to 4% W doping. This is consistent with the XANES result that the amount of positive charge of tungsten in TW4 was lower than that in TW2. As such, the unique structure of W-doped TiO_2 containing cation (Ti) and anion (O) vacancies and dangling oxygen could lead to an increase of photothermocatalytic activity of the catalysts as seen in the catalytic result (Figure 3-1d). The higher tungsten doping concentration in TW4 leads to higher amounts of these active catalytic sites, resulting in higher catalytic activity. Meanwhile, TW10 has two W-O shells in the EXAFS fitting results, with the W-O shell at a longer distance caused by the formation of WO_3 outside of the TiO_2 lattice. This result can also be seen in the XRD results (Figure 3-1c), where smaller peaks different than the main peaks were found as a result of the formation of WO_3. The formation of WO_3 inhibits the photocatalytic CO_2 reduction, due to the conduction band of WO_3 being lower than that of TiO_2, which causes electrons trapped by the O defects to flow to the

WO$_3$ conduction band, as discovered in the source work. Due to this, decreased photothermocatalytic properties were observed for TW10 compared to TW4.

3.3.3 XAS Analysis of Ti K-edge

For the XANES spectra of the Ti K-edge, as shown in Figure 3-4, there was little change in white line intensity of the four samples, an indication that the four samples share similar electronic properties. It was confirmed that the structure of Ti had a slight disturbance when W doping into TiO$_2$. As such, Ti vacancies were responsible for the neutral charge, and therefore, dangling oxygen was produced due to bonding with Ti vacancies.
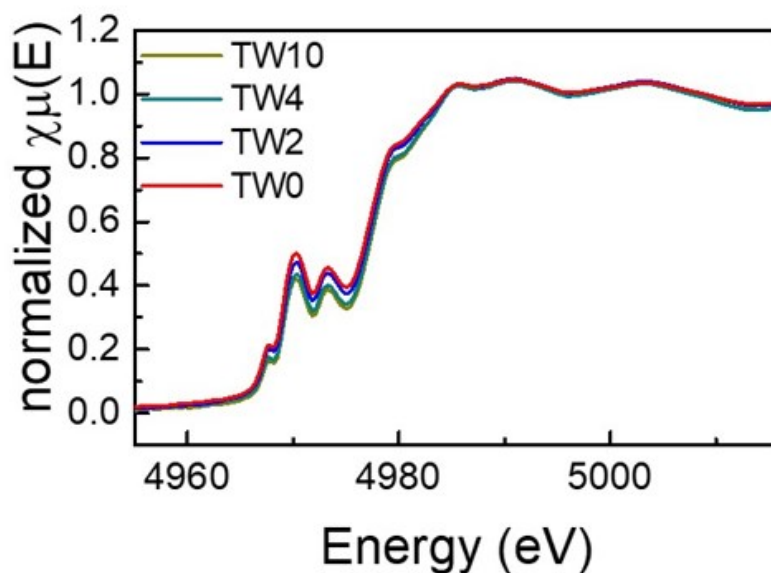
Figure 3-4: Ti K-edge FT-EXAFS Spectra of TW0, TW2, TW4, and TW10

The Ti K-edge EXAFS spectra are shown in Figure 3-5. The major EXAFS peak in the region from 1-2 Å CN comes from the first shell of the Ti-O bonds. As shown in Table 3-2, the CN increases proportional to the concentration of doped tungsten. The CN of bulk rutile TiO$_2$

has an expected value of 6. The CN of the undoped samples, TW0, is lower at 5.0, which may

be a result of both being a nanomaterial as well as possible oxygen defects being present.

TiW10, which shows little change in CN compared to TiW4, is an exception to the observed

trend of CN from the three other samples. This is in agreement with the XRD results, in which

WO_3 is shown to form and aggregate beyond a 4% W doping concentration. As the W-dopant

concentration increased, more of such low CN Ti sites will be replaced by tungsten. As a result,

the CNs of Ti-O increased with increased W-doping concentration.

Table 3-2: Ti K-edge EXAFS Fitting Results of W-doped TiO_2 Samples Scanned in Transmission

Mode

Sample	Shell	CN	R (Å)	σ^2	E_0	R-Factor
TW0	Ti-O	5.0 (8)	1.95 (2)	0.003 (2)	11 (2)	0.009
TW2	Ti-O	5.5 (9)	1.96 (2)	0.003 (3)	12 (2)	0.016
TW4	Ti-O	6 (1)	1.95 (2)	0.003 (3)	12 (2)	0.011
TW10	Ti-O	6.1 (6)	1.95 (1)	0.003 (1)	12 (1)	0.003

S_0^2 has been set to 0.16 based on averaging of data
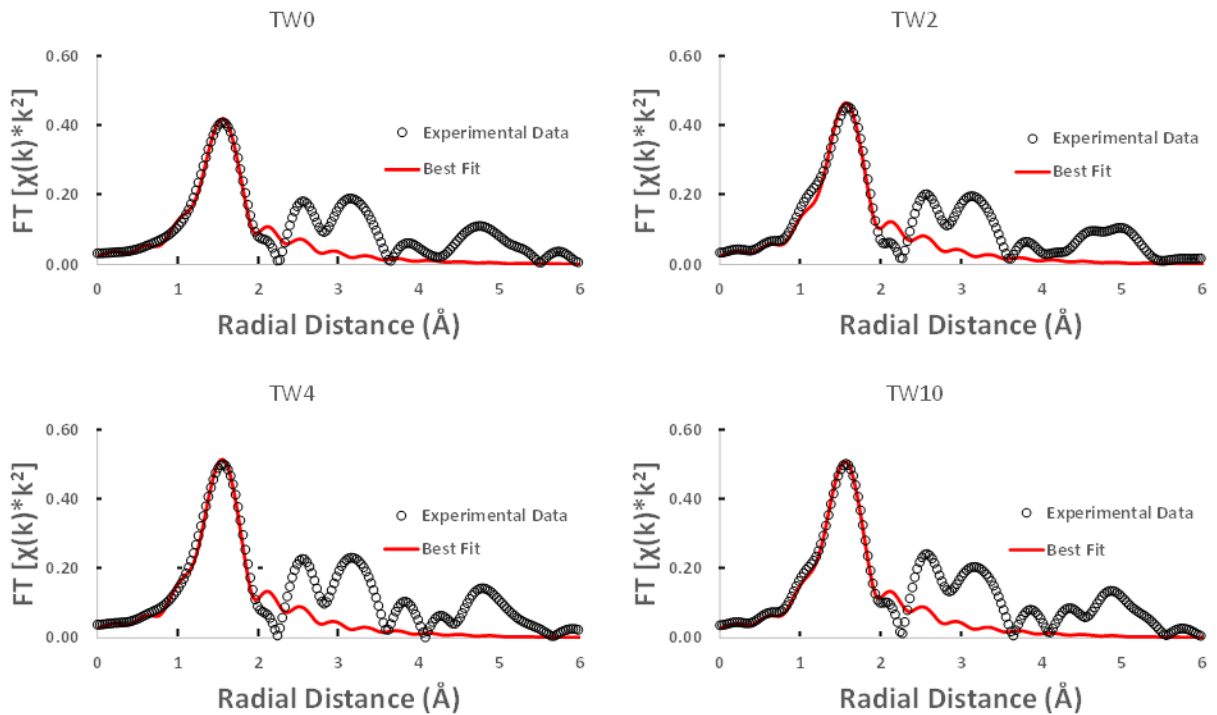
Figure 3-5: Ti K-edge FT-EXAFS Spectra of TW0, TW2, TW4, and TW10 Samples

3.3.4 Mechanism of Reaction

Based on the results of the Ti K-edge analysis, as well as results from the W L_{III}-edge analysis, it can be determined that, when W was doped into TiO_2, Ti vacancies and dangling oxygen atoms were generated, and the dangling oxygen atoms would either remain or escape to form oxygen vacancies in the lattice during heating in the synthesis. The amount of Ti vacancies and defective oxygen atoms increased proportional to the W dopant concentration. A mechanism for the reaction is proposed in Figure 3-6.
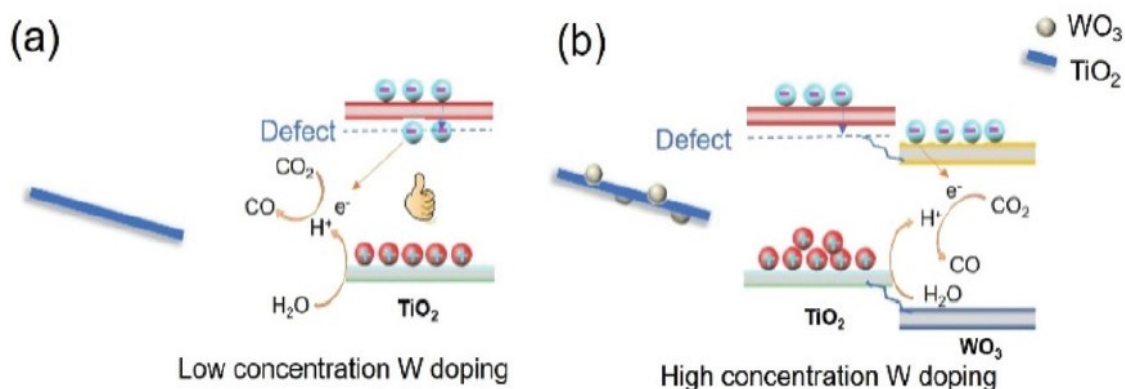
Figure 3-6: Scheme of W-doped TiO_2 over (a) low and (b) high doping concentrations. Relative energy level positions of TiO_2 and WO_3 were estimated for illustration purposes.

When low concentration of W was doped into TiO_2, W replaced Ti in the TiO_2 lattice. To keep the charge neutrality, Ti vacancies were generated. At the same time, the oxygen bonded with Ti vacancies became dangling oxygen. The dangling oxygen and related oxygen vacancies were beneficial for CO_2 absorption and charge transfer. In addition, new energy levels were formed in the band gap acting as electron trapping centres to prolong the charge carrier lifetime (Figure 3-6a).[65] Both of these two aspects improve the photothermocatalytic reaction of CO_2 with H_2O. Therefore, the catalytic activity of TW2 was significantly improved relative to TW0.

Upon increasing the doping concentration from 2% to 4%, more Ti atoms were replaced by W atoms, which resulted in more Ti vacancies. This can be seen from the result of the Ti-K edge fitting. The amount of dangling oxygen and the number of oxygen vacancies near the W centres also increased. Since the amount of catalytically active sites of oxygen vacancies and dangling oxygen increased, the catalytic activity of TW4 was further improved. Upon increasing

the W doping concentration to 10%, the extra W species that were not doped into the TiO_2

lattice aggregated to form WO_3. Since the conduction band of WO_3 was lower than that of TiO_2,

electrons trapped by the O defects flowed to the WO_3 conduction band (Figure 3-6b).

Consequently, the catalytically active O sites cannot be used for the reaction, inhibiting the

photocatalytic CO_2 reduction. As such, the photothermocatalytic properties of TW10 decreased

in comparison with TW4.

3.4   Conclusion

In conclusion, XANES and EXAFS were utilised to better understand the atomic structure

and bonding properties of the W-doped catalysts. It was shown that the replacement of

titanium with tungsten dopant resulted in the formation of titanium vacancies to maintain the

charge neutrality of the semiconductor. As a result, dangling oxygen and oxygen vacancies

were generated and acted as catalytically active sites for catalytic reduction. TW4 was the most

catalytically efficient catalyst, demonstrated by the formation of WO_3 that occurs when 10% W

is introduced in the system, seen in the EXAFS fitting results of the W L_{III}-Edge. In addition to

other characterization methods performed, XAS allowed for deeper analysis into the structure

of the nanocatalysts and understand the strength of doping.

Chapter 4: X-ray Absorption Spectroscopy Analysis of Manganese Cobalt Oxide Nanocatalysts Supported on Carbon Nanotubes

Contributions: Tingting Zhao (University College London, U.K.) performed synthesis and non-XAS characterization of all samples. David Do collected the XAS data, conducted the XAS analysis and produced the XAS result discussion.

4.1 Introduction

Bimetallic transition-metal/metal oxide nanoparticles have received considerable attention in the area of electrocatalysis due to their high chemical and thermal stability, their ability to be supported on a carbon nanotube structure, and, most notably, their bifunctionality, allowing them to be tuned for use in both the oxygen evolution reaction (OER) and the oxygen reduction reaction (ORR).[66–71] Bimetallic $Mn_xCo_{3-x}O_4$@NCNTs have shown promise for acting as a nanocatalyst for energy storage as they contain multicomponent metal oxides, allowing for improved electron hopping and enriched metal-ion redox couples. In addition, both cobalt and manganese are abundant metals, making them an attractive choice for catalysis over less abundant metals.[72]

In this chapter, using XAS, the hybrid structure has been studied in detail, allowing for further tuning of the catalyst for long-term applications in oxygen electrocatalysis. X-ray analysis, supported by TEM imaging as well as PXRD data, is performed on five samples of varying amounts of cobalt and manganese, measuring both the cobalt and manganese K-edges. Close examination of the structural bonding of each sample allows for greater understanding of how the atomic structure changes as the ratio of manganese and cobalt changes, and, consequently, their practicality as nanocatalysts.

4.2   Experimental Methods

4.2.1   Synthesis of Electrocatalysts and General Characterization Methods

The synthetic procedures for the development of manganese cobalt oxide/nitrogen-doped multiwalled carbon nanotube hybrids are detailed in previous work by Zhao et al.[72] The procedure involves dispersing pre-oxidized carbon nanotubes in ethanol uniformly, and adding aqueous solution precursors of the two metals used, which were $(CH_3COO)_2Co \bullet 4H_2O$ and $(CH_3COO)_2Mn \bullet 4H_2O$. The product was collected with centrifugation and freeze-dried to obtain the final product. Morphology and elemental analysis of samples were conducted using TEM (JEOL-2100F), and phase and structure was determined using PXRD (STOE StadiP) by using $Mo_{K\alpha}$ radiation ($\lambda = 0.71$Å).

4.2.2   X-ray Absorption Spectroscopy and Data Analysis

EXAFS analysis was performed on eight of the synthesized metal carbon nanotube hybrids, as well as four samples of the tungsten-doped TiO_2 samples. Measurements were performed at the Argonne National Laboratory's Advanced Photon Source Sector 20-BM and Sector 9-BM, at the manganese K-edge (6539 eV), the cobalt K-edge (7709 eV), and the tungsten L_3-edge (10207 eV). Powder samples of the electrocatalysts were packed on Kapton tape, which was folded multiple times to increase the concentration. Samples that were low in powder quantity were instead packed into a washer and folded over with Kapton tape.

Linear combination X-ray absorption spectroscopy was performed using the WinXAS data analysis program.[49] Both cobalt and manganese fits were performed, based on the data of $Mn_{1.5}Co_{1.5}O_4$, using a range of 7.70 – 7.76 eV and 6.53 – 6.59 eV, respectively. EXAFS data

analysis was performed using the Athena and Artemis XAS analysis programs.[53] Manganese

and cobalt foil measurements were performed simultaneously with sample measurements for

reference. *K*-ranges of 3.4-12.4 Å^{-1} and 3.2-11.2 Å^{-1}, as well as R-windows of 1.2-3.5 Å and 1.2-

3.6 Å, were used for the fittings of cobalt and manganese data, respectively.

4.3   Results and Discussion

4.3.1   Results of Non-XAS Characterization Methods

As can be seen in Figure 4-1, the Powder X-ray Diffraction results indicate that $MnCo_2O_4$

has a fully cubic atomic structure, due to its pattern closely resembling that of Co_3O_4, which is a

known cubic structure standard.[73] The Mn/Co ratio determines the crystallographic phase

structure of the $Mn_xCo_{3-x}O_4$ nanotubes, where x > 1.5 yields a tetragonal structure, and x < 1.5

yields a cubic structure, resulting in different catalytic properties.[74–76] Figure 4-2 depicts TEM

images of all five samples analyzed, showing a clear increase in the nanoparticles size as the

concentration of manganese increased within the samples. In particular, there is a large

increase in nanoparticle size as the ratio of manganese increases from x = 1.5 to x = 2. This is an

indication of a shift in the structure of the bimetallic compound, providing further evidence of

the phase change that occurs (from cubic to tetragonal).
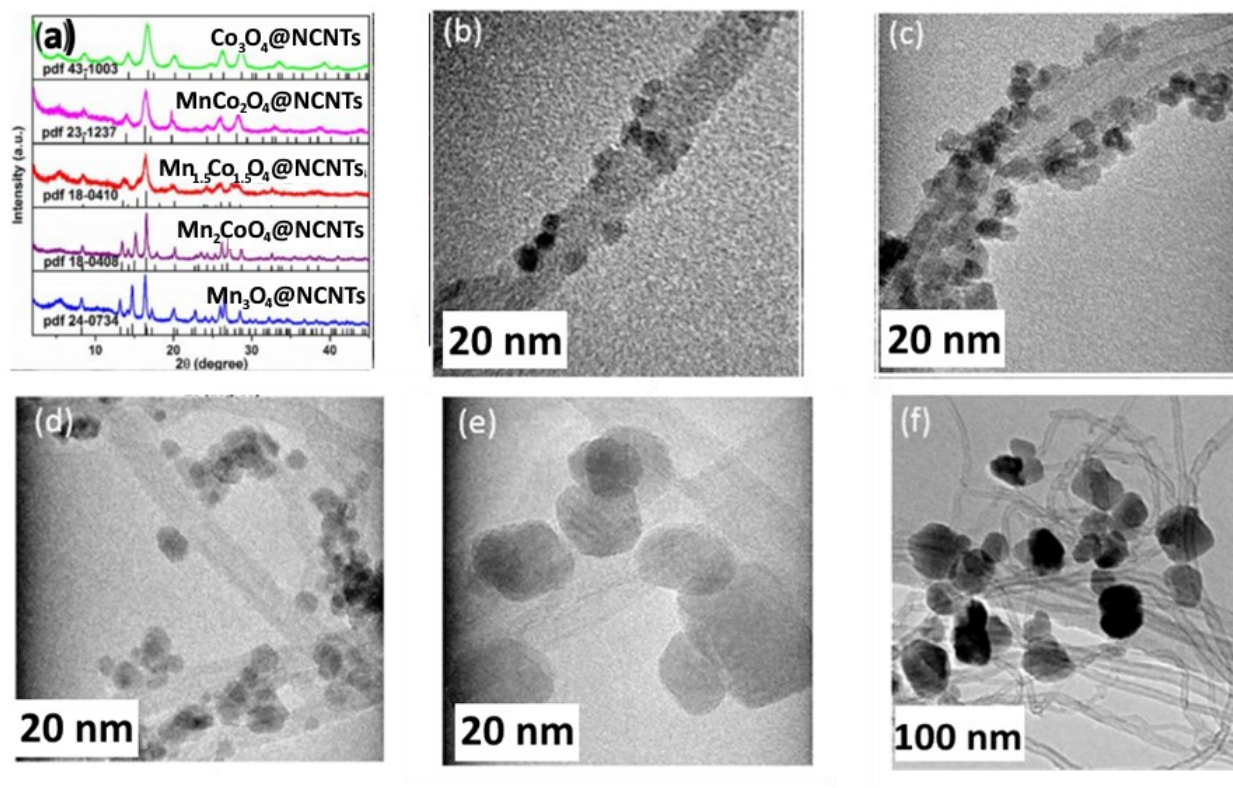
Figure 4-1: (a) PXRD Patterns of MCO@NCNTs, and TEM images of b) Co_3O_4@NCNT [3 – 5 nm],

c) $MnCo_2O_4$@NCNT [3 – 5 nm], d) $Mn_{1.5}Co_{1.5}O_4$@NCNT [10 – 20 nm], e) Mn_2CoO_4@NCNT [10 –

20 nm], and f) Mn_3O_4@NCNT [50nm].

4.3.2 EXAFS Results of $Mn_xCo_{3-x}O_4$ (Manganese K-Edge)

Comparing the initial metal-oxygen shell (the peak that lies between 1 and 2 Angstroms,

typically a region showing metal-nonmetal interactions[45]) shows that the determined

coordination number of oxygen atoms to manganese, within error, sees a downward trend as

the manganese content increases for each sample. This indicates that, as a higher manganese

content increases the size of manganese nanoparticles, there is a decrease in the active surface

area of the nanocatalyst, and as such, there are weaker interactions between the nanocatalyst

and adsorbed oxygen. There is also a general upward trend of the coordination number when compared to the Mn-Mn coordination numbers as the amount of manganese content in a sample increases, also indicative of an increased amount of manganese (and as such, less manganese-oxygen interaction).

As the manganese content decreases within each sample, both the first and second shell Mn-O coordination number values also increase, rising from 3.4 and 1.3 (Mn_3O_4), respectively, to 3.8 and 1.6 (Mn_2CoO_4), a pattern that can also be observed in the cobalt K-edge data (Table 4-2). A dramatic increase in the Mn-O first shell coordination number can be observed from x = 2 to x = 1.5, rising from 3.8 to 5, a point at which, based on the dramatic increase mentioned, a transition from a tetragonal phase to a cubic phase is possible to have occured and metal-oxygen interactions are more favourable.[77–79] Also of note is the Mn-O first shell bond distance, which decreases as manganese content is lost (from 1.95 Å in Mn_3O_4 to 1.89 Å in $MnCo_2O_4$), due to the phase transition from a tetrahedral phase structure (longer bond length of metal-oxygen, about 2.037 Å in bulk Mn_3O_4) to a cubic structure (shorter bond length of metal-oxygen, about 1.948 Å in bulk Co_3O_4).

Furthermore, the Mn-Mn first shell bond distance also sees a decrease as manganese content decreases, from 2.95 Å (Mn_3O_4) to 2.93 Å (Mn_2CoO_4), again due to a phase transition, where the metal-metal bond distance shortens due to the shift in phase, where cubic metal-metal bond distances are shorter than the tetrahedral bond distances. Of note are the second and third Mn-Mn shells, which display large discrepancies compared to the bulk reference. This is likely a result of long-range order being lost as a result of the nanosize effect[80] (the

41

nanoparticles are much smaller in size compared to bulk material) leading to a larger variation

in long distance bonding relative to the reference.

Table 4-1: EXAFS Fitting Results for **$Mn_xCo_{3-x}O_4$** with respect to manganese K-Edge. Bulk

reference data for **$MnCo_2O_4$** is derived from Co_3O_4 data.

Sample	Shell	C.N.	C.N. Bulk	R (Å)	R (Å) Bulk	σ^2 (Å^2)	ΔE_0 (eV)	R-Factor
Mn_3O_4	Mn-O	3.4 (7)	4	1.95 (2)	1.962	0.007 (2)	4 (3)	0.019
	Mn-O	1.3 (5)	4	2.33 (4)	2.074			
	Mn-Mn	2 (1)	2	2.95 (3)	2.938			
	Mn-Mn	5 (2)	4	3.18 (2)	3.172			
	Mn-Mn	5 (2)	8	3.46 (2)	3.496			
Mn_2CoO_4	Mn-O	3.8 (3)		1.923 (5)		0.0058 (6)	2.8 (7)	0.002
	Mn-O	1.6 (3)		2.29 (1)				
	Mn-Mn	3.2 (3)		2.955 (8)				
	Mn-Mn	5.4 (5)		3.156 (7)				
	Mn-Mn	4.0 (5)		3.408 (7)				
$Mn_{1.5}Co_{1.5}O_4$	Mn-O	5 (1)		1.89 (3)		0.008 (4)	-6 (4)	0.022
	Mn-O	1.6 (9)		2.3 (2)				
	Mn-Mn	3 (2)		2.93 (4)				
	Mn-Mn	2 (2)		3.44 (7)				
	Mn-Mn	2 (2)		3.74 (7)				
$MnCo_2O_4$	Mn-O	5 (2)	6	1.89 (2)	1.930	0.0008 (2)	-6 (2)	0.003
	Mn-O	2 (2)	4	2.10 (6)	1.953			
	Mn-Mn	4.1 (8)	6	2.91 (2)	2.877			
	Mn-Mn	1.8 (7)	12	3.43 (3)	3.374			
	Mn-Mn	1.5 (9)	4	3.77 (4)	3.524			

The unit cells of bulk Mn_3O_4, which contains a tetragonal phase structure[78,81], and bulk

Co_3O_4, which is a cubic phase structure, are shown in Figure 4-3. Based on the results obtained

from EXAFS analysis of the Mn K-edge, as the amount of Co increases, Co atoms occupy sites

that were previously filled with Mn, with tetrahedral sites being occupied first. More

manganese sites are replaced by cobalt as the cobalt content increases, eventually undergoing

a phase transition to a cubic phase material.
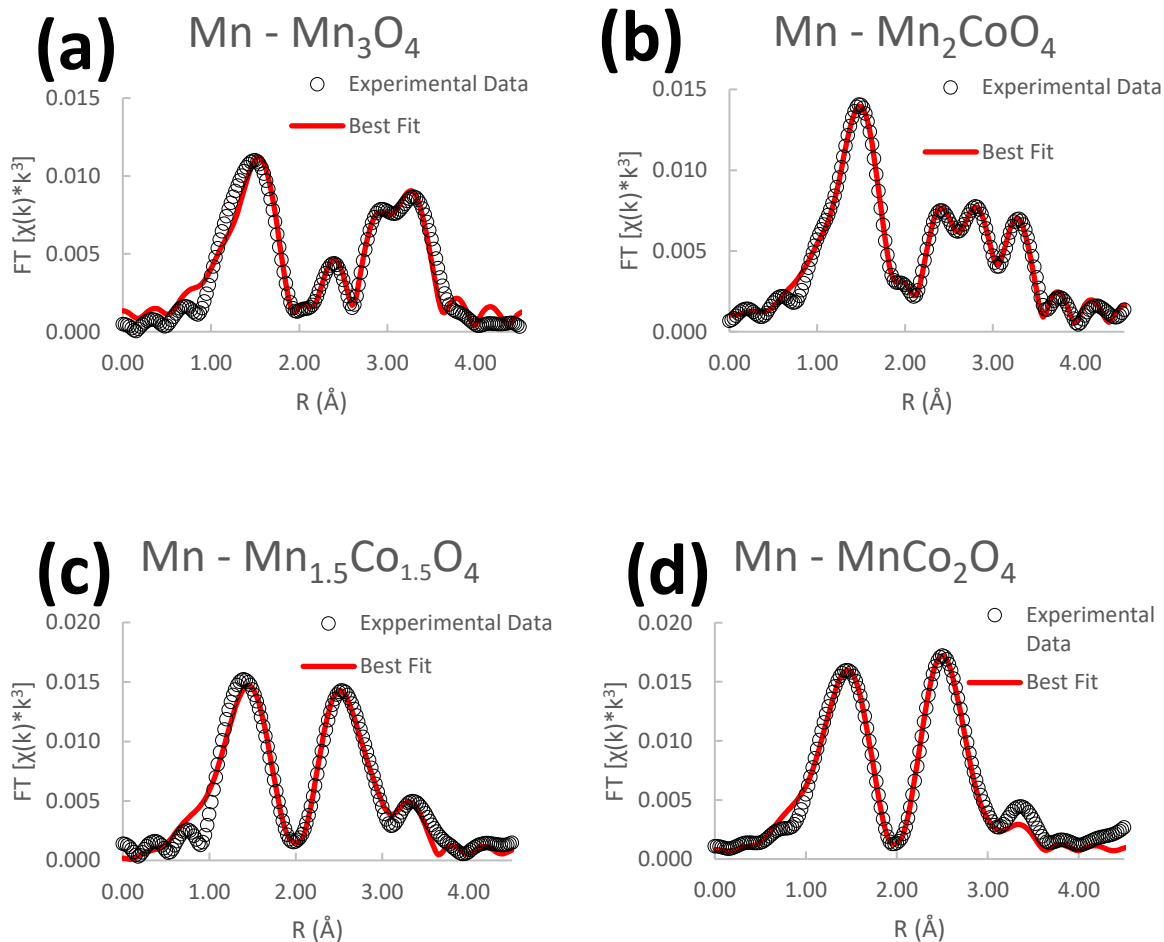
Figure 4-2: Fitted Fourier Transform EXAFS data of (a) Mn$_3$O$_4$, (b) Mn$_2$CoO$_4$, (c) Mn$_{1.5}$Co$_{1.5}$O$_4$, and (d) MnCo$_2$O$_4$ with respect to manganese K-Edge
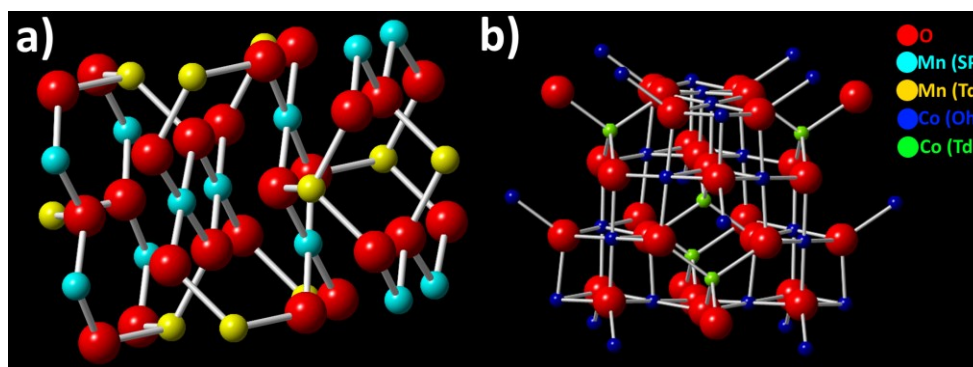
Figure 4-3: Unit Cell model of bulk (a) Mn$_3$O$_4$ and (b) Co$_3$O$_4$.

4.3.3   EXAFS Results of $Mn_xCo_{3-x}O_4$ (Cobalt K-Edge)

Results obtained from the fitting of the four analyzed bifunctional nanocatalysts can be seen below in Table 4-2. Similar to the trends observed within the fitting results for the manganese edge samples, the cobalt K-edge samples also display values indicating the strength of the $MnCo_2O_4$ bifunctional nanocatalyst in comparison to the others tested. As the cobalt content decreases (this is equivalent to an increase in manganese content), the coordination number of the first shell cobalt-oxygen interaction decreases as well. This is likely due to the phase transition from cubic to tetrahedral, shifting from a coordination number of about 6 (cobalt octahedral sites) to 4 (manganese-oxygen sites). The bond distance of the Co-O shell also notably increases as the manganese content increases, with a sharp jump for the Mn_1Co_2 sample in particular. This is consistent with a phase transition (cubic to tetragonal) occurring at that ratio. The cubic metal-oxygen bond length is roughly 1.953 Angstroms, and the manganese metal-oxygen bond length is about 2.037 Angstroms, which is in agreement with the bond length measured for the Co_1 sample (2.00 Angstroms), providing further evidence for a phase transition.

The first shell Co-Co bond distance also shows a slight increase as manganese content increases – this may also be a result of the phase transition, as tetrahedral structures for metal-metal bonds have noticeably longer bond lengths than cubic bond lengths. The second and third-shell Co-Co values for bond distance and coordination are noticeably varied in value – as was the case with the Mn K-edge analysis, this is likely a result of a loss of long-range order in the system due to the small size of the nanoparticles (nanosize effect) and as such, large uncertainty is to be expected. By looking at the fitted Fourier Transform EXAFS spectra below

(Figure 4-4), one can also see that a noticeable change in the shape of the metal-metal region occurs for the latter two samples – this is also due to the crystallographic phase shift (cubic into tetrahedral).

Table 4-2: EXAFS Fitting Results for **$Mn_xCo_{3-x}O_4$** with respect to Cobalt K-Edge. Bulk reference data for **Mn_2CoO_4** derived from Mn_3O_4.

Sample	Shell	C.N.	C.N. Bulk	R (Å)	R (Å) Bulk	σ^2 (Å^2)	ΔE_0 (eV)	R-Factor
Co_3O_4	Co-O	4.4 (1)	4.41	1.91 (2)	1.948	0.002 (2)	-7 (3)	0.011
	Co-Co	4.3 (3)	6	2.88 (3)	2.77	0.004 (5)		
	Co-Co	3.2 (2)	12	3.20 (7)	3.374			
	Co-Co	1.7 (2)	4	3.42 (9)	3.524			
$MnCo_2O_4$	Co-O	4.2 (2)		1.93 (2)		0.003 (3)	-6 (4)	0.014
	Co-Co	5.9 (6)		2.89 (9)		0.008 (1)		
	Co-Co	4.0 (2)		3.1 (2)				
	Co-Co	3.4 (5)		3.45 (6)				
$Mn_{1.5}Co_{1.5}O_4$	Co-O	3.5 (6)		1.94 (1)		0.004 (2)	5 (1)	0.011
	Co-Co	2.7 (8)		2.91 (2)		0.008 (3)		
	Co-Co	5 (2)		3.27 (2)				
	Co-Co	1.4 (9)		3.65 (7)				
Mn_2CoO_4	Co-O	3.1 (9)	4	2.00 (2)	2.037	0.002 (3)	8 (2)	0.022
	Co-Co	1.5 (8)	2	2.91 (3)	2.938	0.005 (4)		
	Co-Co	4.1 (4)	4	3.31 (3)	3.172			
	Co-Co	3.7 (5)	8	3.38 (4)	3.496			
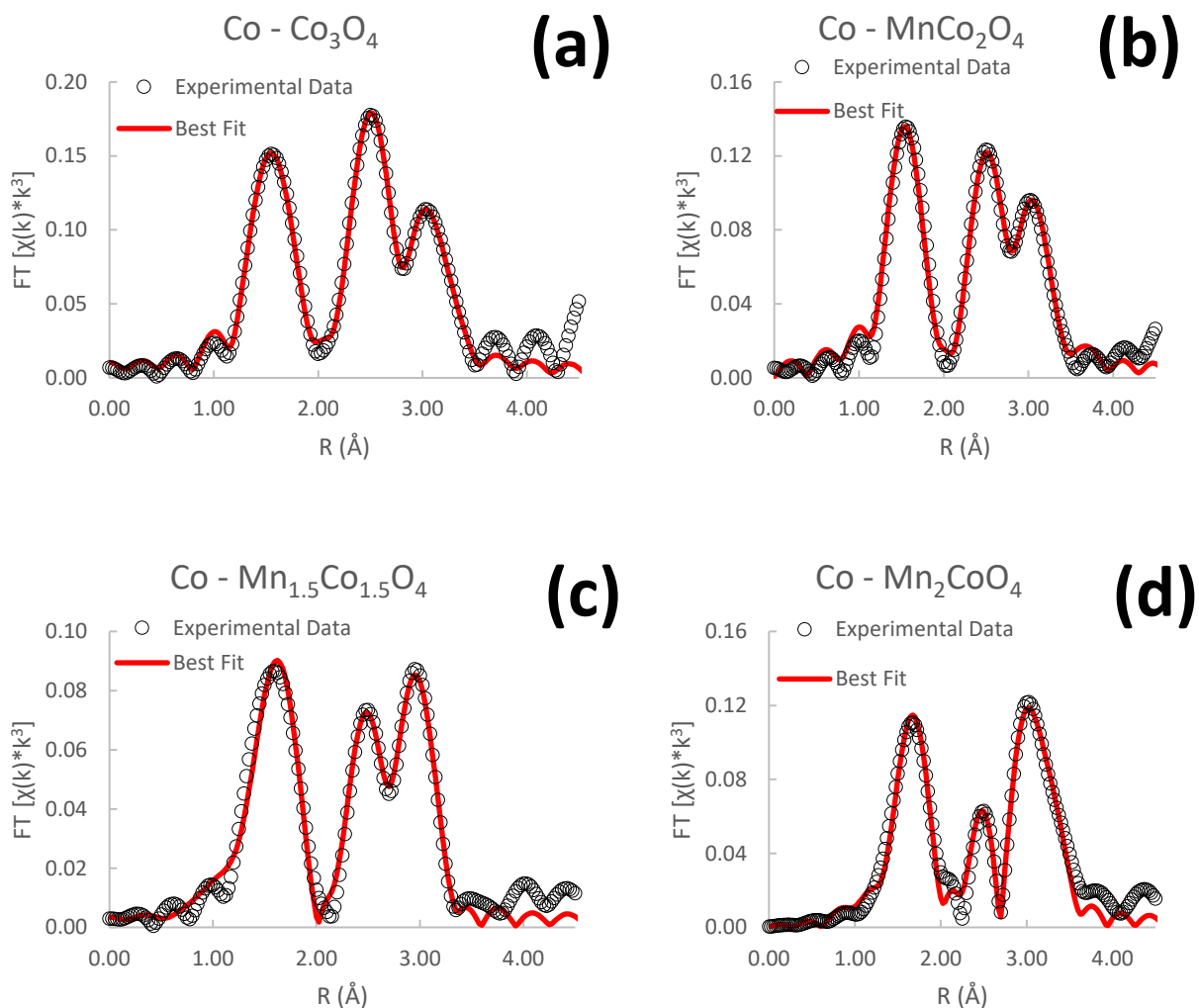
Figure 4-4: Fitted Fourier Transform EXAFS data of (a) Co_3O_4, (b) $MnCo_2O_4$, (c) $Mn_{1.5}Co_{1.5}O_4$, and (d) Mn_2CoO_4 with respect to cobalt K-Edge

4.3.4 XANES Results of $Mn_xCo_{3-x}O_4$

XANES results, obtained from previous research, are shown below (Figure 4-5), where $Mn_{1.5}Co_{1.5}O_4$ has been shown for both the cobalt K-edge and manganese K-edge, alongside standards with known cubic and tetragonal atomic structures. As can be seen from both the Mn K-edge analysis and the Co K-edge analysis, all of the samples containing manganese show

similar absorption edge profiles, indicative of the four samples sharing similar electronic

properties. It can be seen from the Co K-edge XANES spectra that both $Mn_{1.5}Co_{1.5}O_4$ and

$Mn_2Co_1O_4$ are more similar to each other than they are to the reference Co_3O_4. Such a

difference can arise from a phase shift between the samples – as Co_3O_4 has a known cubic

crystal structure, and Mn_3O_4 has a known tetragonal structure, it is at x = 1.5 (an equal Mn and

Co ratio) that a change in structure can be observed.[75,77,81] Furthermore, based on such

observations, it is possible to come to the conclusion that $MnCo_2O_4$ and Mn_2CoO_4 are fully cubic

and tetragonal, respectively, as the two compounds display similar absorption edge data to the

reference compounds Co_3O_4 and Mn_3O_4, and is documented as such in literature.[78,79] This is

also in agreement with EXAFS analysis, where dramatic shifts in the metal-oxygen coordination

numbers were observed upon comparing $Mn_{1.5}Co_{1.5}O_4$ to the other samples ($MnCo_2O_4$ and

Mn_2CoO_4 for the cobalt K-edge and manganese K-edge, respectively). It should be noted that

the change in oxidation state is relative to the reference compound (Co_3O_4 and Mn_3O_4) and the

overall oxidation state of manganese and cobalt is not significantly affected.
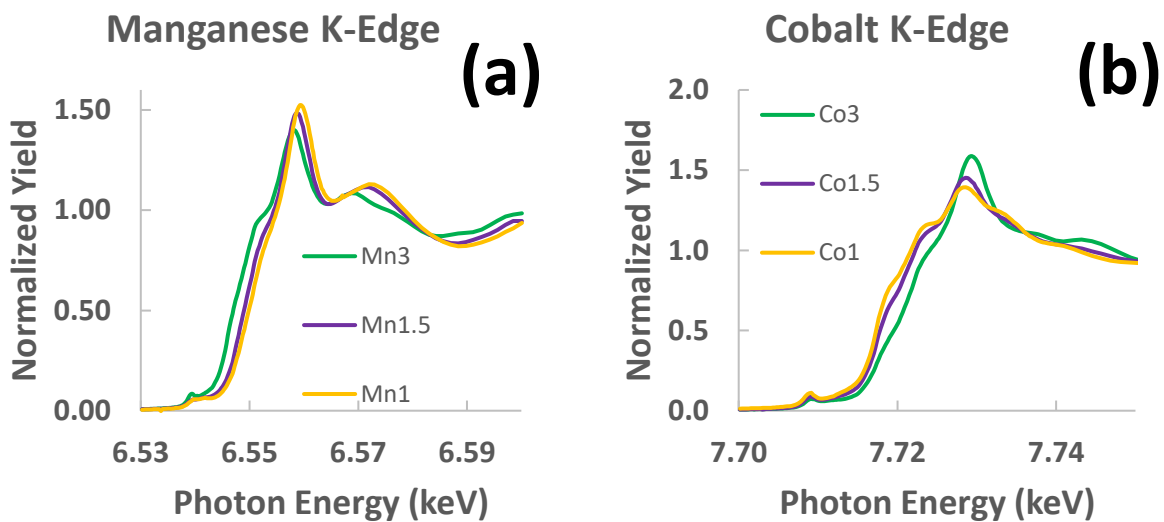
Figure 4-5: XANES Data of $Mn_xCo_{3-x}O_4$ samples for (a) Mn K-Edge and (b) Co K-Edge.

Table 4-3: LC XANES Fit Results of $Mn_{1.5}Co_{1.5}O_4$ for Co K-edge (left) and Mn K-edge (right).

	Co₃ (Cubic)	Co₁ (Tetragonal)	Mn₃ (Tetragonal)	Mn₁ (Cubic)
Partial C	0.349	0.631	0.203	0.788
E₀ Shift	-0.000745	0.000271	0.00135	-0.000768
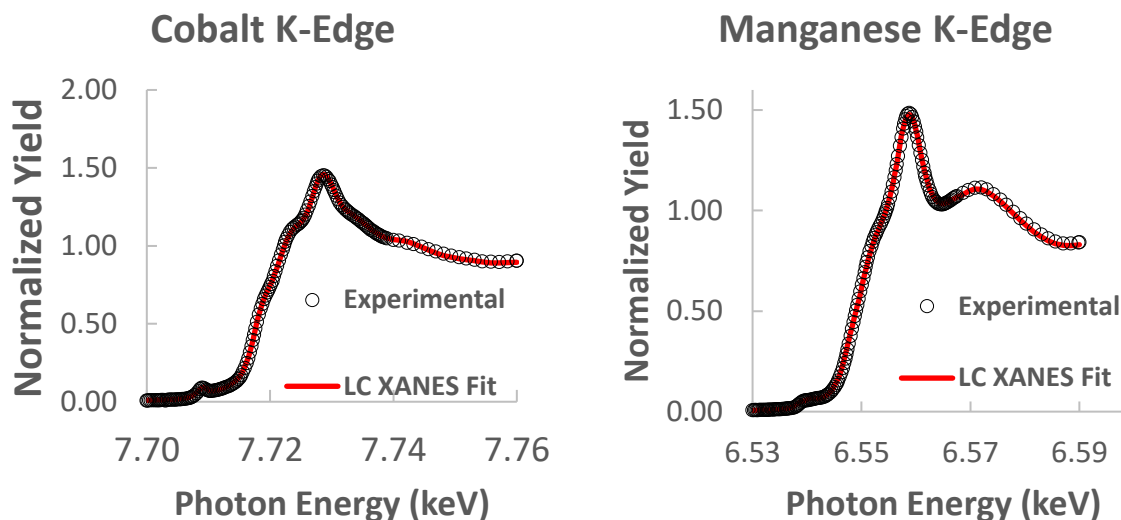
Figure 4-6: Linear Combination X-Ray Absorption Near-Edge Spectroscopy Fit Data of

$Mn_{1.5}Co_{1.5}O_4$ samples for (a) Co K-Edge and (b) Mn K-Edge.

A linear combination (LC) XANES Fit was also performed in order to determine the

relative amounts of cubic phase and tetragonal phase content within the $Mn_{1.5}Co_{1.5}O_4$ sample,

where the phase change is observed to occur based on observations from the XANES data, the

results of which can be seen in Figure 4-6 and Table 4-3. Based on data obtained from PXRD,

the atomic structures of $MnCo_2O_4$ and Mn_2CoO_4 were assumed to be completely cubic and

tetragonal in structure, respectively, and as such were used as reference during linear

combination XANES fitting.

From the results shown in Table 4-3, it can be observed that $Mn_{1.5}Co_{1.5}O_4$ is a dual-phase

material, consisting of both cubic and tetragonal phases.[74,79,82] When examining the cobalt

atoms, a majority of them have converted to the tetragonal phase from the cubic phase.

Similarly, a majority of the manganese atoms have converted from a tetragonal to a cubic

phase. If the respective cubic and tetragonal percentages are added together, values of roughly

1.1 and 0.8, respectively, are obtained. These values are close to 1, providing further evidence

of a dual-phase material, but the slight variation from 1 indicates that the bimetallic samples

are not perfect representations of cubic and tetragonal atomic structures. This is also in

agreement with the EXAFS analysis, where the $Mn_{1.5}Co_{1.5}O_4$ sample showed significant change

in bonding properties when examined from both the cobalt edge and the manganese K-edge.

Starting from the fully tetragonal Mn_3O_4, when cobalt is introduced into the atomic

structure, it is likely that some of the manganese active sites are replaced with cobalt atoms;

due to the large shift from tetragonal to cubic observed in the LC XANES fitting, it is likely that

the square planar sites are being occupied, as they comprise the majority of the Mn-O sites. As

an equal ratio of manganese and cobalt is reached, cobalt sites shift from an expected oxygen

coordination number of 4 (tetrahedral bulk coordination) to 6 (cubic bulk coordination)[83],

resulting in the dual-phase that is observed. When the amount of cobalt exceeds that of

manganese, the atomic structure transitions to that of a cubic, resembling Co_3O_4.

4.4   Conclusion

Joint use of both XANES and EXAFS, supported by characterization techniques such as

TEM imaging and XRD, allowed for deeper understanding of the underlying atomic structure

and its changes in the manganese cobalt oxide samples. EXAFS analysis of $MnCo_2O_4$ and

Mn_2CoO_4 was performed in order to observe changes in the atomic structure, as the two

structures were assumed to be completely cubic and tetragonal, respectively. The increasing

manganese content in each sample showed a decrease in cobalt-oxygen first-shell coordination,

an increase in manganese-oxygen first-shell coordination, and an increase and decrease in the

metal-metal bond distances of cobalt and manganese, respectively, all of which are consistent

with a transition from a cubic phase structure to a tetragonal phase structure. A clear

transition from a cubic phase (with no manganese content) to a tetragonal phase (having no

cobalt content) was made more apparent in the analysis of $Mn_{1.5}Co_{1.5}O_4$, where a dual-phase

structure was observed, based on results from linear combination XANES fitting, with both

edges showing that there was a mixture of both cubic and tetragonal phases. Greater

understanding of the changing atomic structure using these methods may allow for better fine

tuning of the materials, and consequently, their practical use in real-world applications.

Chapter 5: X-ray Absorption Spectroscopy Analysis of Monometallic and

Bimetallic Ruthenium Nanoparticles on Zeolites

Contributions: Ziyi Chen (Dalhousie University,) performed TEM Imaging for samples. All other work was conducted by David Do.

5.1   Introduction

Metal nanoparticles have received considerable attention as catalysts, exhibiting high catalytic activity in various reactions, such as hydrogenation[17,84] and oxidation.[85,86] However, due to the small size of metal nanoparticles, their stability is often an issue when utilised under more extreme reaction conditions.[87] As such, one method of overcoming such a drawback is to deposit the metal nanoparticles on an inorganic support, which also has the benefit of preventing the nanoparticles from aggregating (which would result in a decrease of catalytic activity due to increased size). Zeolites in particular are well-studied materials that can act as a support for metal nanoparticles, being crystalline, microporous materials that have nearly uniform arrays of porous sites to accommodate them, which, in addition to enhancing the stability of metal nanoparticles, can also serve as an active support through a synergistic effect by acting as a co-catalyst.[88–91]

In this chapter, ruthenium nanoparticles deposited on three different large pore zeolites with varying structures (Y, Beta, and Mordenite) are closely examined, the structures of each zeolite being seen in Figure 5-1. Zeolite Y, beta, and mordenite have pore sizes of 0.74 nm[92], 0.67 nm[93], and 0.70 nm[94], respectively. TEM imaging was performed to view the nanoparticles on the zeolite surfaces, and XAS was used for better understanding of the atomic structure. Furthermore, the concentration of ruthenium was altered to better understand the effect it

may have on the catalytic activity. Depositing another metal (the 3d metal cobalt and the 4d

metal palladium) along with the ruthenium, creating a bimetallic nanoparticle system, was also

performed in order to examine possible changes to the electronic structure and bonding

properties.[95,96] Using XAS analysis, in addition to supporting evidence provided by other

characterization methods, it is possible to better understand the atomic structure of the metal

nanoparticles on a zeolite support, and such information can allow for better tuning of the

structure and properties of metal nanocatalysts.
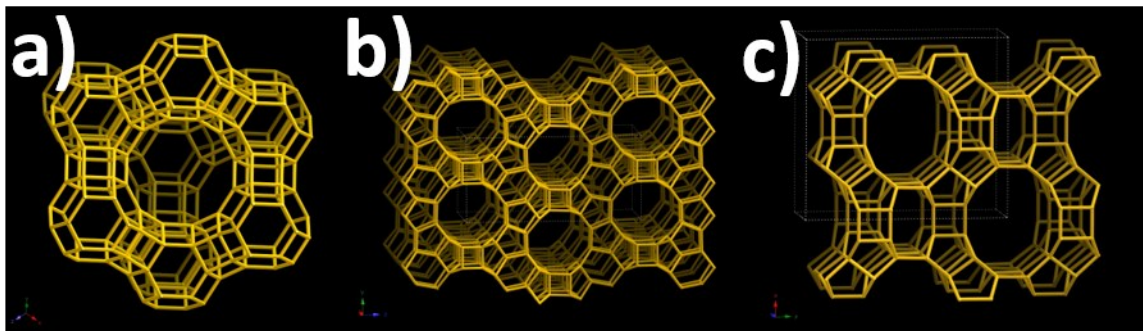
Figure 5-1: Framework of a) Y, b) Beta, and c) Mordenite zeolites[75]
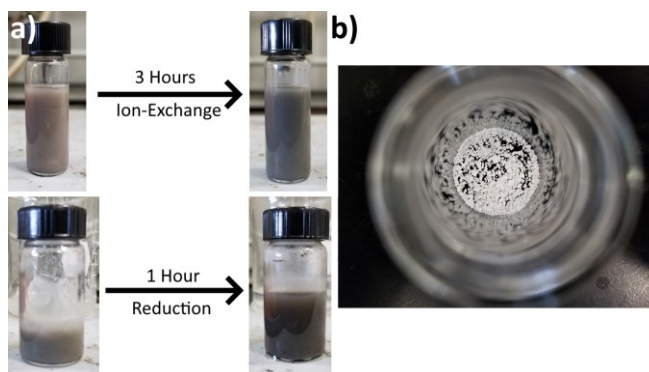
Figure 5-2: a) Ruthenium/Cobalt on zeolite sample after both ion-exchange and reduction steps

and b) Ruthenium/Cobalt bimetallic sample on Y zeolite, collected after drying in oven for 24

hours

5.2 Experimental Methods

5.2.1 Synthesis of Ruthenium Samples on Zeolite

The synthesis of the metal nanoparticles is described herein. A metal stock solution for each of ruthenium, cobalt, and palladium was prepared by obtaining a precursor metal compound, dissolving a small amount of each in deionized water, and transferring to a volumetric flask to obtain a 10 mmol/L solution for each.[85] The metal precursors used in this experiment were $RuCl_3 \bullet H_2O$, $CoSO_4 \bullet xH_2O$, and $Pd(NH_3)_4Cl_2$.

0.1 g of zeolite powder was then dissolved in 1 g of deionized water. The zeolite solution was then injected with one of the metal stock solutions (two, if preparing a bimetallic sample) using a micropipette, with the amount injected varying depending on the weight percent of 0.1 g. In this experiment, weight percentages of 0.1, 0.2, 0.5, 0.8, and 1.0 were used to vary concentration. When comparing the effect the zeolite has on the sample, a 1.0 wt% sample was used to compare each. Bimetallic samples were performed with 0.5 wt% as the standard for a 1:1 solution. The volume required was determined through conversion of the weight percent to mols of element, and as such, 494.5 µL of ruthenium and palladium stock solution was used for 0.5 wt%.

The solution was then checked to make sure the pH was below 10 to avoid precipitation, and then placed in an oil bath for 3 hours in order to undergo the ion-exchange process, heated at a controlled 80°C with constant stirring on a hot plate. Afterwards, the solution was washed with deionized water and centrifuged three times with water, and then once with ethanol, using a Beckman Coulter Allegra Z-22R Centrifuge at 15000 RPM for 10 minutes each, decanting

and sonicating in-between each use. Afterwards, the solid powder is dissolved in 2 g of deionized water and sonicated again.

During the centrifuge process, a sodium borohydride solution dispersed in deionized water was prepared. Typical reductants are added to maintain a constant 1:10 molar ratio of metal/NaBH$_4$, but this experiment used 0.08 g of NaBH$_4$ in order to elicit a stronger response, as previous experiments did not show signs of reduction. The reducing solution was split into two parts (3 g and 5 g) to be added separately to the zeolite solution. The zeolite solution, in a glass vial, was placed in a constantly stirred ice bath for 1 hour to undergo reduction, wherein 3 g of NaBH$_4$ solution was slowly added, and after 10 minutes, 5 g of NaBH$_4$ was added. Solution was capped and placed under a nitrogen environment to attempt to prevent oxidation of metals. The reduction process typically involves a noticeable colour change. The solution was then treated to the same centrifuging procedure outlined after the ion-exchange step, and then left to dry in an oven at 60°C for 24 hours, after which the powder was collected, weighed, and stored. Example images of the ruthenium and cobalt zeolite solution (with three times the amount of cobalt to ruthenium) after both ion-exchange and reduction can be seen in Figure 5-2 (a), and the resulting powder after drying can be seen in Figure 5-2 (b).

5.2.2   X-ray Absorption Spectroscopy and Other Characterization Methods

XAS measurements were conducted and obtained using the Sector 9-BM and Sector 20-BM beamlines at the Advanced Photon Source at Argonne National Laboratory (Argonne National Laboratory, IL). Powder samples were measured by packing powder in washers supported and sealed on Kapton tape for the purpose of adequate X-ray absorption. All

samples were measured in fluorescence mode. Known metal foil references of ruthenium and palladium were measured concurrently with each sample. Scans were performed at the ruthenium K-edge, the palladium K-edge, and the cobalt K-edge. At least five scans were performed for each sample, under ambient conditions at room temperature.

XAS data processing and fitting for the ruthenium nanoparticles was performed with data processing programs Athena and Artemis.[53] As known metal foils were measured, it was possible to determine the amplitude reduction factor, S_0^2, by fixing known coordination number (CN) values. A k-weighting of 2 was applied for all samples. The monometallic ruthenium, bimetallic ruthenium-cobalt samples, and all bimetallic ruthenium palladium Pd K-edge samples were fitted using a k-space of 2.5-10.0. For Ru K-edge bimetallic ruthenium-palladium samples, k-spaces of 2.5 – 12.0 and 2.5 – 9.5 were used for Y and Mordenite samples, respectively.

Transmission Electron Microscopy was also performed on five different samples, those being three monometallic ruthenium samples (one on each of the Y, beta, and mordenite zeolites) as well as two ruthenium/cobalt samples (the equal ratio samples on Y and beta). A TECNAI F-30 high-resolution microscope at 300 kV in Xiamen University, which is equipped with a field-emission electron gun, was used to perform TEM experiments. All samples were dispersed in ethanol and ultrasonicated before being casted onto a copper grid as a drop-casted suspension. After drying the grid to evaporate the solvent, the samples were measured by examining select areas at different magnifications. Due to the COVID-19 pandemic, TEM images of the ruthenium/palladium bimetallic samples could not be obtained due to those samples being prepared later than the monometallic and bimetallic ruthenium/cobalt samples.

5.3   Results and Discussion

5.3.1   Monometallic Ruthenium on Zeolite XAS Analysis

The TEM images for each monometallic sample are shown in Figure 5-3. It can be seen for ruthenium on the Y zeolite that the formation of nanoparticles and nanoclusters has occurred, indicated by the dark dots that are of different colour than the lighter zeolite surface that are roughly 2 nm in size.[97] Similar observations can be made when examining the TEM images for both beta and mordenite. Notably, unlike the beta and mordenite images, the dark dots on the Y zeolite lack a clear shape, indicating possible differences between it and the other two zeolites. The images show that there are possible metal-metal interactions taking place that can be studied using XAS spectroscopy.
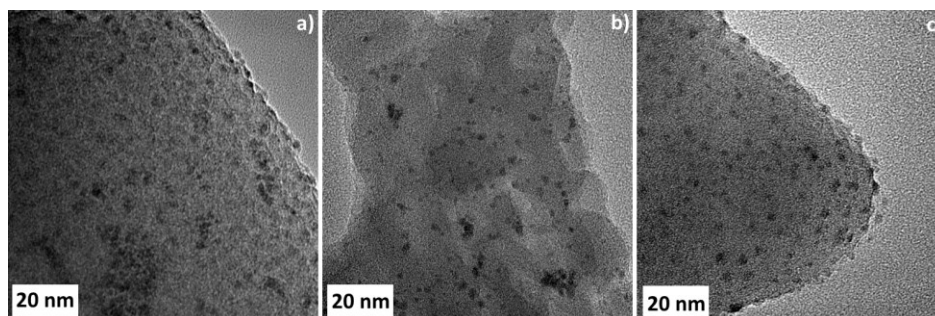
Figure 5-3: TEM Images of a) Ru 1.0wt% on Y, b) Ru 1.0wt% on Beta, c) Ru 1.0wt% on mordenite

Figure 5-4a and 5-5a display the XANES data graphs of monometallic ruthenium on zeolites, when varying the concentration and zeolite, respectively. It can be seen in the XANES data for both that the ruthenium on zeolite samples have a noticeably different shape compared to that of the bulk foil reference sample, an indication of a difference in the electronic properties between the two. The XANES data of the bulk foil contains a doublet that

is characteristic of metallic bonds, whereas the tall, wide peaks of each ruthenium on zeolite sample is more distinctive of ionic bonding. Noticeably, compared to both the beta and mordenite zeolites (Figure 5-5a), ruthenium on Y zeolite had a higher white line intensity, indicative of greater ionic character (as a result of a higher oxidation state on ruthenium) and, consequently, less metallic character that would be expected in XAS analysis of nanoparticles on zeolite. Figure 5-4b and 5-5b display the EXAFS data of the monometallic ruthenium samples on zeolite, where the lack of a metal core, indicated by the lack of a clearly defined metal-metal peak beyond 2 Å, is in agreement with the different XANES white line shapes previously observed. The peak intensity of the metal-oxygen peak between 1 – 2 Å decreases as the ruthenium concentration decreases, which would indicate lower amounts of ruthenium oxidation as the concentration decreases, but the lack of a metallic bond suggests that the concentration for the monometallic ruthenium samples has little effect on its structural properties. When comparing each zeolite instead, the samples prepared on beta and mordenite show similar properties, both having much less intense metal-oxygen interactions and more metallic character compared to the sample prepared on Y, seen by the more distinct peak in the metal-metal interaction region. It should be noted that the ruthenium-ruthenium peak seen in the reference foil FT-EXAFS is much more intense than the peaks displayed by those of the nanoparticle samples, indicative of a vastly lower coordination number for that bond, which is to be expected of nanoparticles compared to the bulk.

The EXAFS fittings results shown in Table 5-1 support the qualitative observations made based on Fourier transformed data. Surface oxidation is highest for the sample on Y, shown by the high Ru-O shell coordination number of 5, compared to coordination numbers of 3 and 3.5

for mordenite and beta, respectively. No metallic bond could be observed for the monometallic

sample on Y, showing its lack of a metal core, whereas the other two samples do show a Ru-Ru

shell bond with a low coordination number, both having a CN of roughly 2, compared to the

bulk coordination number of 12 for a hexagonal closed-pack crystal structure. The resulting

structure would be small, with a triangular-shape structure for the ruthenium bonds, and with

ruthenium atoms being coordinated to about 3 oxygen atoms in the beta and mordenite

samples, it would result in the Ru-Ru bonds being longer due to small expansion. This can be

seen in the Ru-Ru bond distance for both samples, which are longer than 2.65 Å, the bond

distance of Ru-Ru in bulk ruthenium.[98]
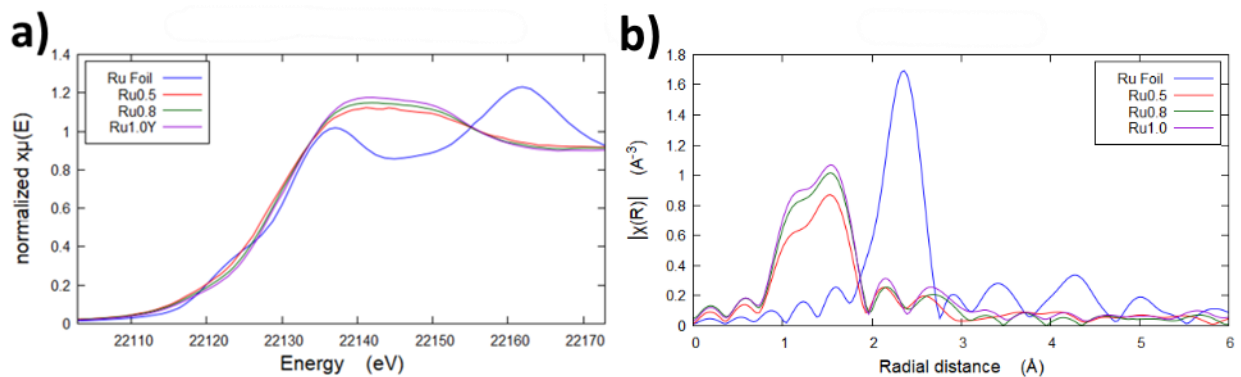
Figure 5-4: a) XANES data graph and b) EXAFS-FT data graph of ruthenium on Y, varying

concentration (0.5 wt%, 0.8 wt% and 1.0 wt%), with Ru foil FT-EXAFS data at 0.25% intensity.

Monometallic ruthenium with weight percent 0.1 and 0.2 omitted due to no noticeable

difference to 0.5.
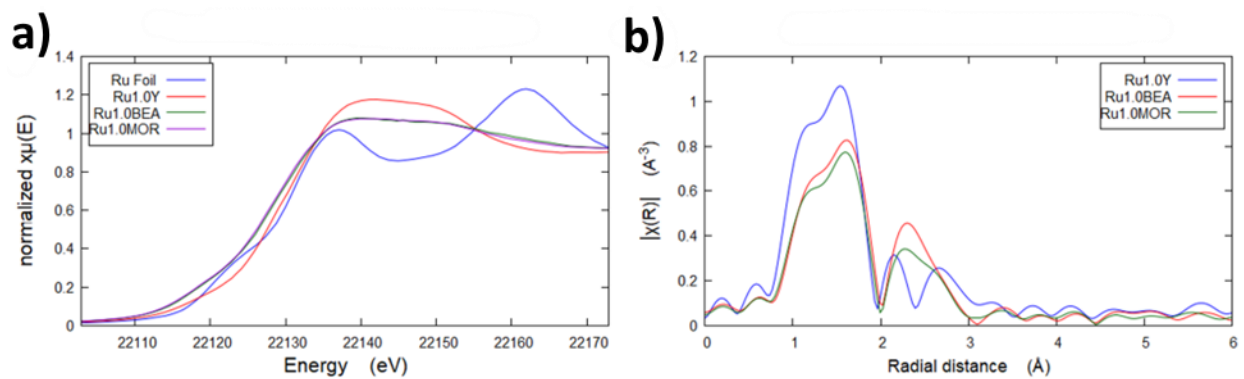
Figure 5-5: a) XANES data graph and b) EXAFS-FT data graph of ruthenium 1.0wt% on varying

zeolites. Ruthenium foil data not included due to its much larger intensity.
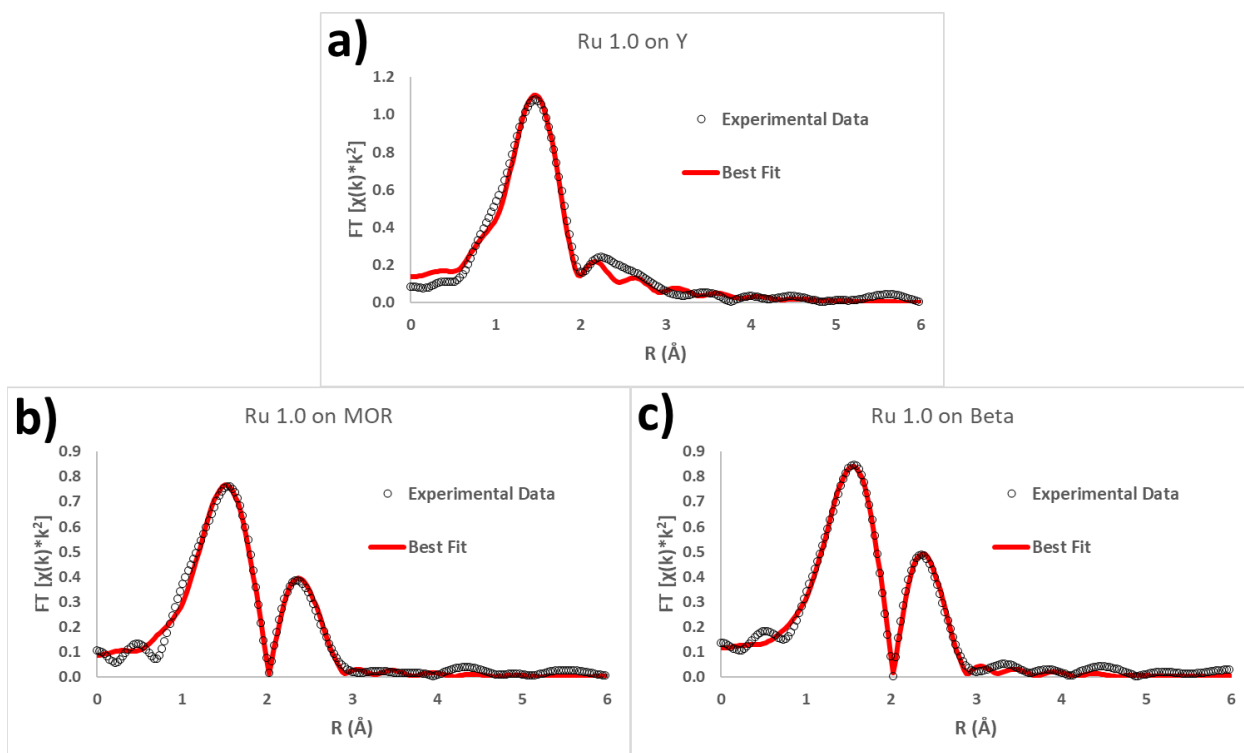
Figure 5-6: Fitted Fourier Transform EXAFS data of monometallic Ru on a) Y, b) mordenite, and

c) beta

Table 5-1: EXAFS Fittings Results for Monometallic ruthenium on zeolite samples

Sample	Shell	C.N.	R (Å)	σ^2 (Å²)	ΔE_0 (eV)	R-Factor
Ru1.0wt% on Y	Ru-O	5 (1)	2.02 (3)	0.006 (4)	1 (4)	0.008
Ru1.0wt% on Mordenite	Ru-O	3 (1)	2.02 (3)	0.006 (5)	0 (4)	0.010
	Ru-Ru	2 (2)	2.70 (4)	0.009 (7)	-3 (5)	
Ru1.0wt% on Beta	Ru-O	3.5 (5)	2.007 (2)	0.007 (2)	4 (2)	0.002
	Ru-Ru	2.3 (8)	2.68 (2)	0.008 (3)	-1 (2)	

5.3.2   Bimetallic Ruthenium / Cobalt on Zeolite XAS Analysis

The TEM images for two of the bimetallic samples are shown in Figure 5-7. It can be seen for ruthenium / cobalt on Y zeolite that little dispersion of the metal nanoparticles has occurred. Conversely, the ruthenium and cobalt nanoparticles on the beta zeolite are easily seen in its TEM image, and the two have clearly distinct surfaces.

As can be seen in Figure 5-8a and Figure 5-9a, the bimetallic samples for ruthenium and cobalt on zeolite with variations in concentration (Ru:Co = 1:1, Ru:Co = 1:3, and Ru:Co = 3:1) all display incredibly similar properties when examined from the ruthenium K-edge. All display a white line in the XANES that is indicative of non-metallic character, lacking a doublet that is seen in the bulk reference foil. Similarly, the EXAFS graphs in Figure 5-8b and Figure 5-9b show near-identical spectra for each, with a large metal-oxygen interaction showing that the metal nanoparticles were likely oxidized during the reduction process, similarly to the monometallic samples. The small peak present in the mordenite samples after the metal-oxygen peak does suggest that a small metal core exists, however.
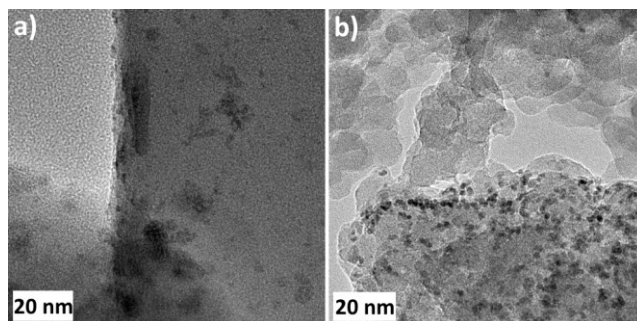
Figure 5-7: TEM Images of a) RuCo 1:1 on Y, b) RuCo 1:1 on Beta
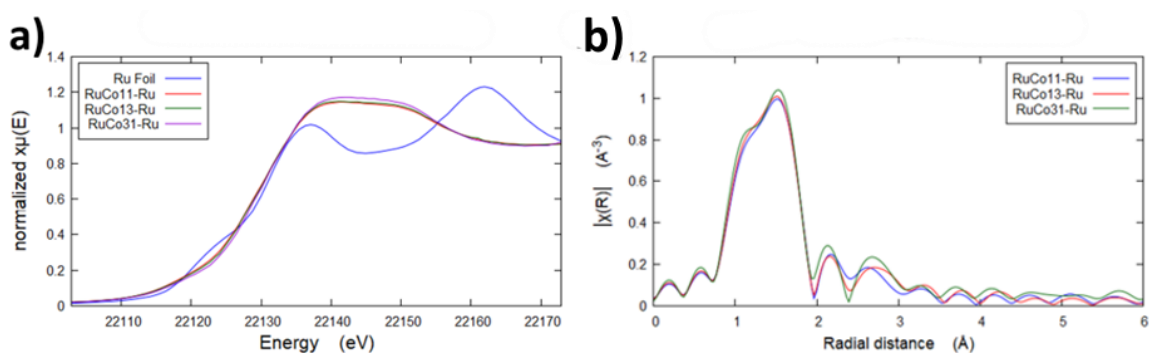
Figure 5-8: a) XANES data graph and b) EXAFS-FT data graph of ruthenium / cobalt on Y, varying

concentration (Ru K-edge)
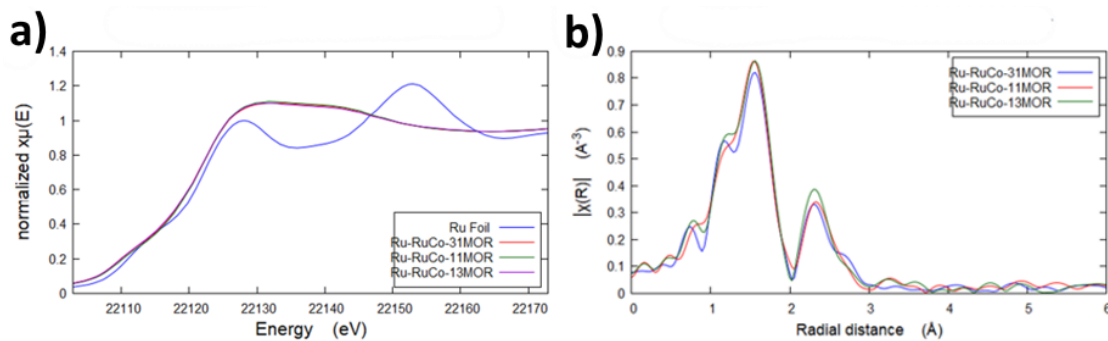
Figure 5-9: a) XANES data and b) EXAFS-FT data of ruthenium / cobalt on mordenite, varying

concentration (Ru K-edge)

The data graphs in Figure 5-8 and Figure 5-9 show that the concentration has little effect on the properties of the nanoparticle sample, whereas changing the zeolite does have a noticeable difference. In particular, the samples prepared on the Y zeolite do not seem to show the formation of a metallic core, whereas the mordenite samples do. This trend is consistent with the monometallic series of samples.

Due to little variation being observed in the XANES and EXAFS data, the EXAFS fitting results shown in Table 5-2 use representative samples for analysis, in which the RuCo (1:1) on Y sample represents all of the bimetallic ruthenium-cobalt samples on Y, and the RuCo (1:1) on mordenite represents all of the mordenite bimetallic samples, as well as the 1:1 sample on beta, which, as can be seen in Figure 5-11b, is incredibly similar to that of the 1:1 sample on mordenite. The EXAFS fitting results display similar findings to that of the monometallic samples, in which the Y zeolite showed a lack of a metal core, whereas the mordenite zeolite does show ruthenium-ruthenium interactions, indicating the presence of a small metal core. Again, for the sample on mordenite, a structure in which there is a small, triangular-like bonding between the ruthenium atoms is present, causing an expansion of the Ru-Ru bond due to the Ru-O bonds present.[99]

When examining the nanoparticle data from the cobalt K-edge perspective, it is apparent that different observations from examining the ruthenium K-edge can be made. The zeolite samples have much less metallic character compared to bulk cobalt, with taller and wider white lines. The EXAFS graphs show that for all of the samples, no metallic core was formed, as well as a significant metal oxide peak, implying significant oxidation occurred during the reduction process. Figure 5-12b and Figure 5-13cd show peaks beyond the expected

metallic core peak region, and due to cobalt being an easily oxidized 3d metal, those peaks are likely indicative of ionic bonds. Such observations indicate that cobalt has little, if any, effect on the metal core seen in the ruthenium K-edge analysis, and as such, EXAFS fitting analysis would provide little information on the structure of the metal nanoparticles on a zeolite.[100]
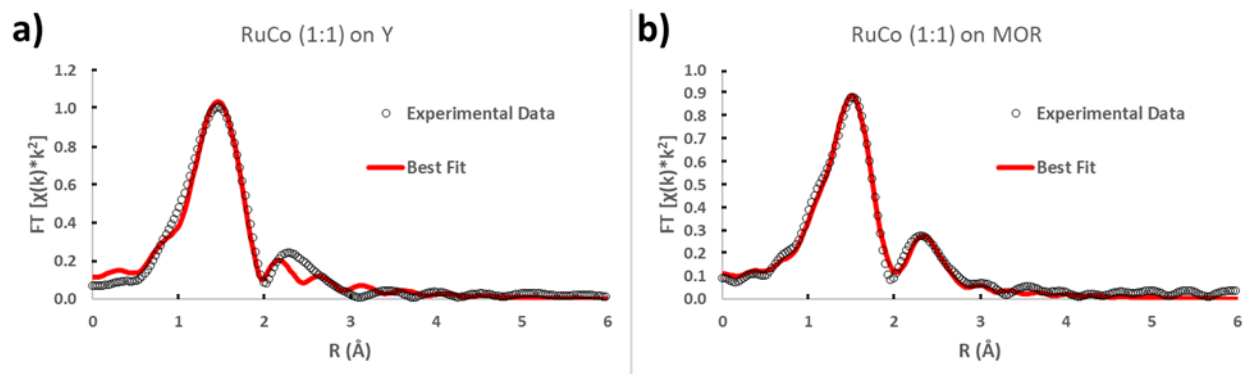
Figure 5-10: Fitted Fourier Transform EXAFS data of bimetallic Ru/Co (1:1) on a) Y and b) mordenite

Table 5-2: EXAFS Fitting Results for bimetallic Ru/Co (1:1) on Y and Mordenite, Ru K-Edge

Sample	Shell	C.N.	R (Å)	σ^2 (Å^2)	ΔE_0 (eV)	R-Factor
RuCo - 1:1 on Y	Ru-O	4 (1)	2.00 (3)	0.004 (4)	-1 (3)	0.016
RuCo - 1:1 on MOR	Ru-O	4.1 (3)	2.028 (8)	0.008 (1)	3.1 (9)	0.008
	Ru-Ru	1.8 (4)	2.69 (2)	0.012 (3)	-1 (2)	
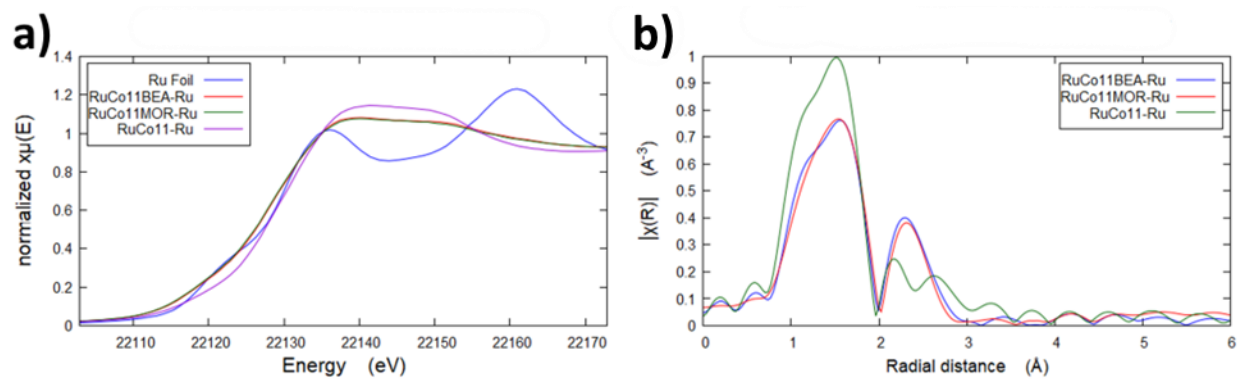
Figure 5-11: a) XANES data and b) EXAFS-FT data of ruthenium / cobalt at equal ratios (Ru K-edge), varying zeolites
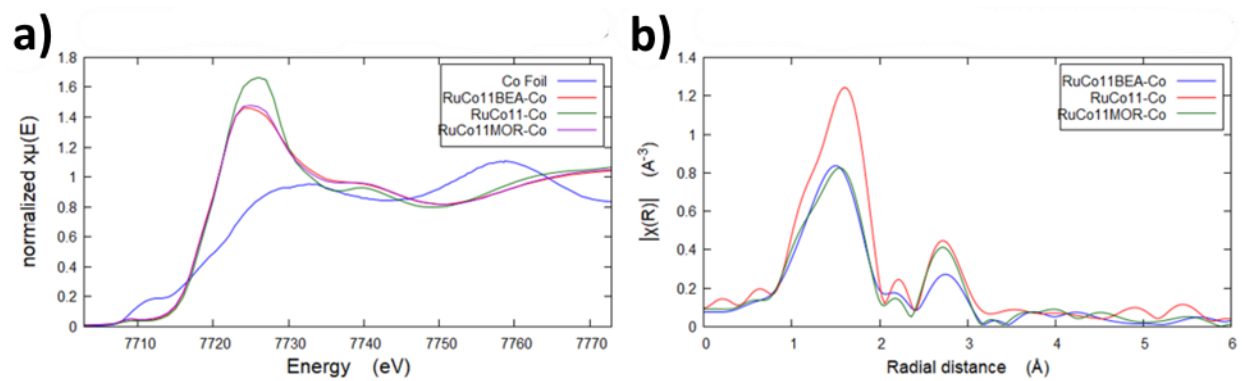
Figure 5-12: a) XANES data and b) EXAFS data of ruthenium / cobalt at equal ratios (Co K-edge), varying zeolites
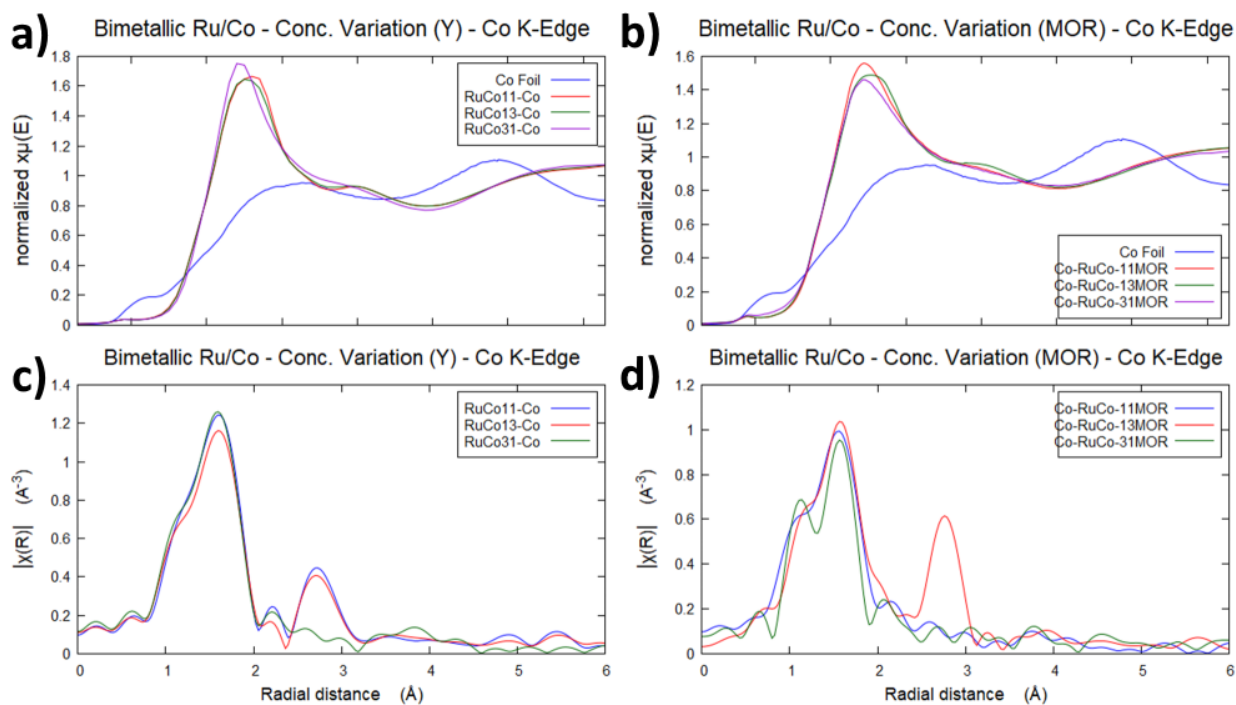
Figure 5-13: XANES concentration variation data graphs (Co K-edge) of a) ruthenium / cobalt on Y and b) ruthenium / cobalt on mordenite and EXAFS concentration variation data graphs (Co K-edge) of c) ruthenium / cobalt on Y and d) ruthenium / cobalt on mordenite

5.3.3   Bimetallic Ruthenium / Palladium on Zeolite XAS Analysis

It can be seen in Figure 5-14a that the XANES graphs that the white lines of the samples are of similar intensity to the bulk metal reference, in contrast to the monometallic ruthenium and bimetallic ruthenium and cobalt samples. The samples lack a doublet that is characteristic of metallic content, but compared to the monometallic samples, which have been included for comparison, the ruthenium and palladium bimetallic samples are less broad and have a lower oxidation state, indicating that the metal nanoparticles more closely resemble the ruthenium foil. This can be further seen in Figure 5-14b and Figure 5-15b, containing the EXAFS, where, although the metal-oxygen peak is still intense, there exists strong metal-metal bond

interaction, indicated by the sharp peak in the region. Notably, the peak increased in intensity with the increase of palladium concentration, indicating that the palladium metal nanoparticles are more prevalent within the system, and contribute more to the bonding to the zeolite.
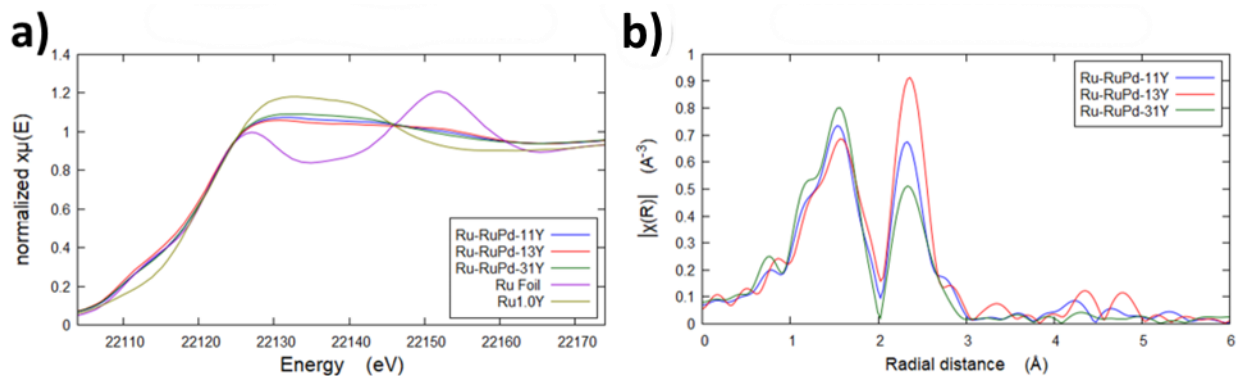
Figure 5-14: a) XANES data and b) EXAFS-FT data of ruthenium / palladium on Y (Ru K-edge), varying concentrations
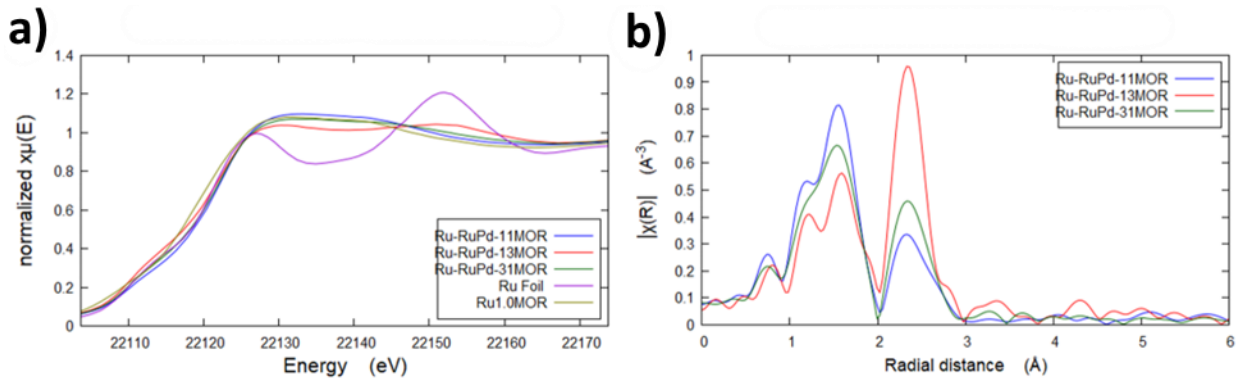
Figure 5-15: a) XANES data and b) EXAFS data of ruthenium / palladium on mordenite (Ru K-edge), varying concentrations

Examining the palladium K-edge in Figure 5-17a and 5-18a shows that the white lines for each sample are less intense compared to the ruthenium/cobalt samples (with reference to their respective metal foil references) and more closely resemble the palladium foil reference,

indicating stronger metallic character than the ruthenium/cobalt samples. The XANES data shows a slight doublet compared to the bulk palladium data for both Y zeolite and mordenite. EXAFS data shows a less intense metal-oxygen peak, as well as a strong, intense metal-metal peak, indicative of metallic character, and as such, a metal core, increasing in intensity as the palladium concentration increased.
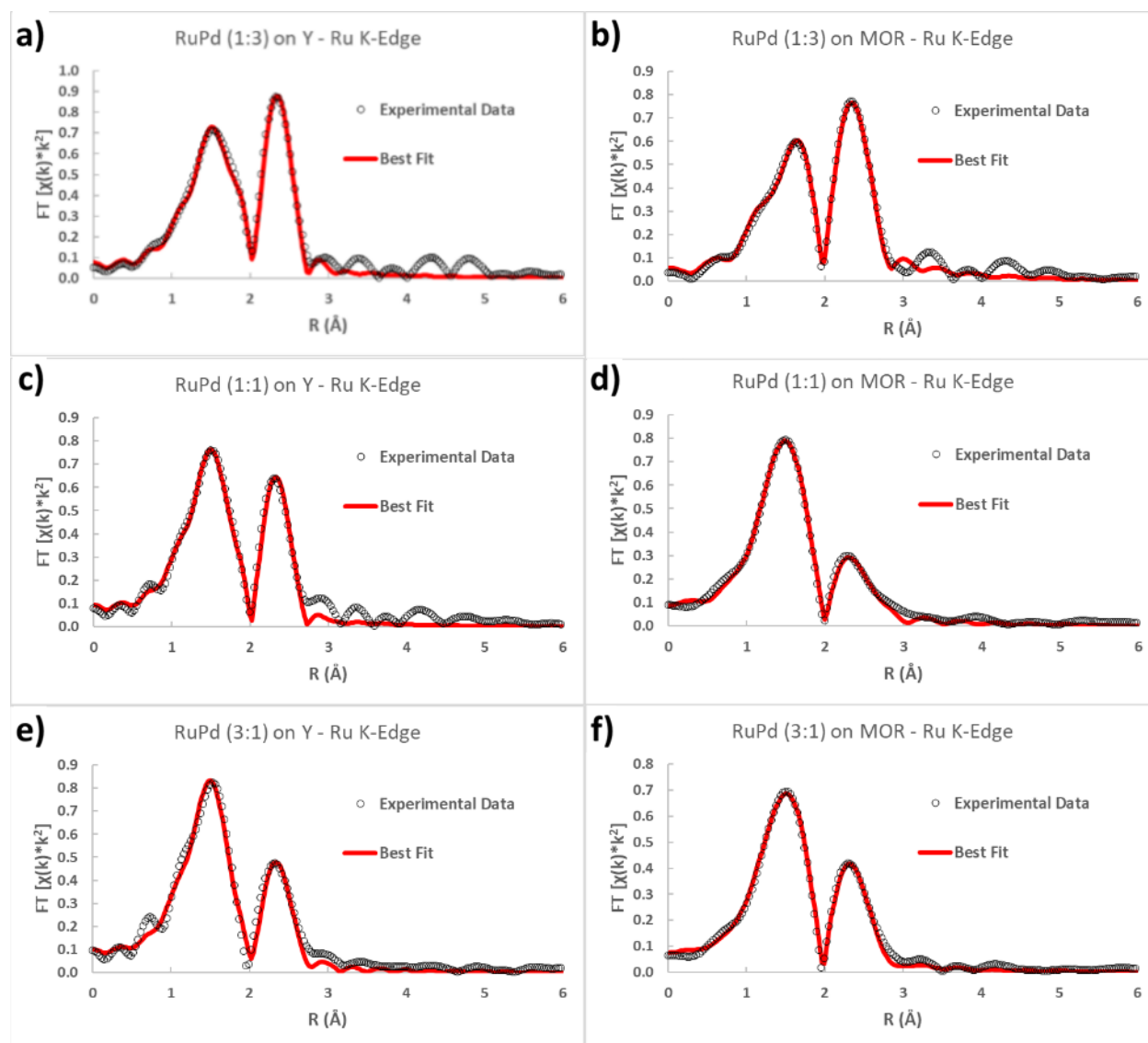
Figure 5-16: Fitted Fourier Transform EXAFS data of bimetallic Ru/Pd (Ru K-Edge) on a) Y (1:3), b) mordenite (1:3), c) Y (1:1), d) mordenite (1:1), e) Y (3:1), and f) mordenite (3:1)

Table 5-3: EXAFS fitting results of Ru K-edge Ru/Pd bimetallic samples on Y with varying concentrations

Sample	Shell	C.N.	R (Å)	σ^2 (Å^2)	ΔE_0 (eV)	R-Factor
RuPdY – 1:3	Ru-O	3.1 (6)	2.03 (2)	0.010 (3)	1 (2)	0.016
	Ru-Ru/Pd	3.6 (6)	2.671 (8)	0.008 (1)	-7 (1)	
RuPdY – 1:1	Ru-O	3.2 (6)	2.02 (2)	0.008 (4)	1 (4)	0.010
	Ru-Ru/Pd	2.8 (7)	2.67 (1)	0.009 (2)	-8 (2)	
RuPdY – 3:1	Ru-O	3.5 (6)	2.02 (2)	0.008 (3)	0 (2)	0.027
	Ru-Ru/Pd	2.5 (8)	2.675 (5)	0.010 (3)	-5 (2)	

Table 5-4: EXAFS fitting results of Pd K-edge Ru/Pd bimetallic samples on Y with varying concentrations

Sample	Shell	C.N.	R (Å)	σ^2 (Å^2)	ΔE_0 (eV)	R-Factor
RuPdY – 1:3	Pd-O	0.8 (7)	2.31 (4)	0.007 (1)	-7.6 (5)	0.002
	Pd-Pd/Ru	7.5 (7)	2.736 (5)	0.008 (1)		
RuPdY – 1:1	Pd-O	1.3 (2)	2.291 (9)	0.005 (3)	-7.5 (2)	0.001
	Pd-Pd/Ru	6.5 (3)	2.733 (2)	0.009 (4)		
RuPdY – 3:1	Pd-O	1.0 (2)	2.06 (2)	0.008 (2)	5 (2)	0.001
	Pd-Pd/Ru	5.4 (3)	2.731 (3)	0.0109 (5)		

The EXAFS fitting results for the samples on the Y zeolite for both the ruthenium and palladium K-edges are shown in Figure 5-16, as well as Tables 5-3 and 5-4. It should be noted that, due to the small difference in atomic number between ruthenium and palladium, it is difficult to distinguish the metal bond as Ru-Ru or Ru-Pd (or Pd-Pd and Pd-Ru), and as such, both are listed. It can be seen from the EXAFS fittings results that a larger metallic core is present compared to the ruthenium-cobalt bimetallic samples, as well as the monometallic samples, due to the Ru-Ru/Pd shell having a more significant coordination number. Furthermore, the results indicate that, as the amount of palladium increases compared to ruthenium, less

oxidation of the sample occurs, due to the coordination number of the Ru-O shell increasing as

the ruthenium ratio increases (from 3.1 to 3.5), as well as a sharp increase in the Pd-Pd/Ru shell

coordination number, showing 7.5 when palladium is three times more concentrated than

ruthenium, and only 5.4 when ruthenium exceeds palladium content by three times. Similar

trends are present when examining the Ru K-edge fitting results. Such results indicate that the

addition of palladium is directly responsible for the larger metal core.

Table 5-5: EXAFS fitting results of Ru K-edge Ru/Pd bimetallic samples on mordenite with

varying concentrations

Sample	Shell	C.N.	R (Å)	σ^2 (Å^2)	ΔE_0 (eV)	R-Factor
RuPdMOR – 1:3	Ru-O	3 (1)	2.03 (4)	0.014 (8)	1 (4)	0.003
	Ru-Ru/Pd	4 (1)	2.67 (1)	0.008 (2)	-8 (1)	
RuPdMOR – 1:1	Ru-O	3.3 (5)	2.02 (1)	0.006 (3)	0 (2)	0.002
	Ru-Ru/Pd	1.5 (7)	2.70 (3)	0.008 (5)	-2 (3)	
RuPdMOR – 3:1	Ru-O	3.0 (7)	2.01 (2)	0.008 (4)	-1 (3)	0.004
	Ru-Ru/Pd	2.2 (9)	2.67 (2)	0.009 (4)	-7 (3)	

Table 5-6: EXAFS fitting results of Pd K-edge Ru/Pd bimetallic samples on mordenite with

varying concentrations

Sample	Shell	C.N.	R (Å)	σ^2 (Å^2)	ΔE_0 (eV)	R-Factor
RuPdMOR – 1:3	Pd-O	1.4 (9)	2.33 (7)	0.01 (1)	-4 (5)	0.001
	Pd-Pd/Ru	6.5 (6)	2.740 (6)	0.009 (1)	-8.4 (7)	
RuPdMOR – 1:1	Pd-O	2.6 (7)	2.28 (1)	0.006 (4)	-7 (3)	0.003
	Pd-Pd/Ru	4.1 (7)	2.73 (1)	0.009 (2)	-4 (1)	
RuPdMOR – 3:1	Pd-O	1.4 (1)	2.07 (1)	0.004 (2)	6 (1)	0.001
	Pd-Pd/Ru	2.6 (3)	2.696 (6)	0.008 (1)	-9.8 (7)	

The fitting results shown from the Tables 5-5 and 5-6, which show both the Ru K-edge

and Pd K-edge of the samples on mordenite, noticeably have a different bond distance for the

Pd-Pd/Ru shell of the RuPdMOR – 1:3 and RuPdMOR – 1:1 samples than expected, especially

compared to the samples in which there is three times the amount of palladium than

ruthenium, at around 2.30 Å. A typical metal-oxygen shell bond distance arising from surface

oxidation has a bond length of about 2.0 Å[101], which is shown in the Ru-PdMOR – 3:1 sample for

the Pd K-edge. The Pd-O shell bond distance can be explained by it being a result of the oxygen

in the zeolite framework, which interacts less strongly than a typical metal-oxygen bond.[102]

Similar results were also present in the samples on Y. In addition, the Pd-Pd coordination

numbers for those samples are vastly higher than the sample with a typical metal-oxygen bond,

which contains much less palladium. Such trends are similar to that of the results seen with the

samples on the Y zeolite. Noticeably, however, the Y zeolite displays higher coordination

numbers for the Pd-Ru/Pd and Ru-Ru/Pd shells compared to the samples on mordenite, which,

as stated previously, is indicative of a larger metal core. This is in contrast with the results seen

from the monometallic and bimetallic ruthenium-cobalt, in which the samples on Y, as indicated

by the lack of Ru-Ru bonding, showed a lack of metallic core formation. Results in literature

show Ru/Pd bimetallic nanoparticle samples show promise as nanocatalysts[103,104], and further

studies should be performed to investigate the catalytic properties of these samples.
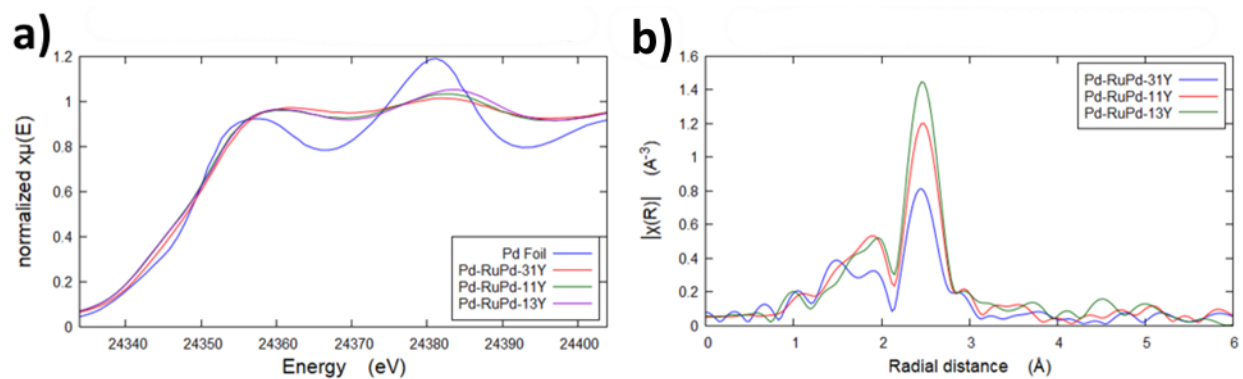
Figure 5-17: a) XANES data and b) EXAFS data of ruthenium / palladium on Y (Pd K-edge),

varying concentrations
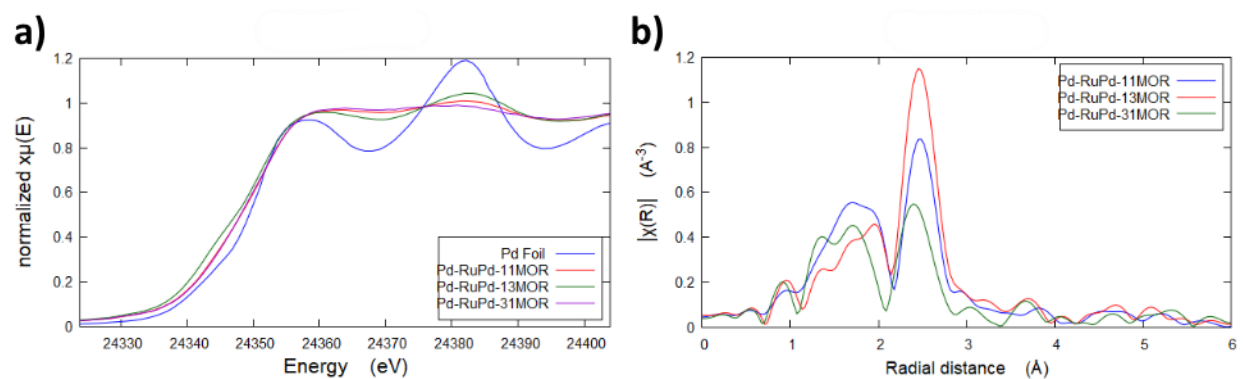
Figure 5-18: a) XANES data and b) EXAFS data of ruthenium / palladium on mordenite (Pd K-

edge), varying concentrations
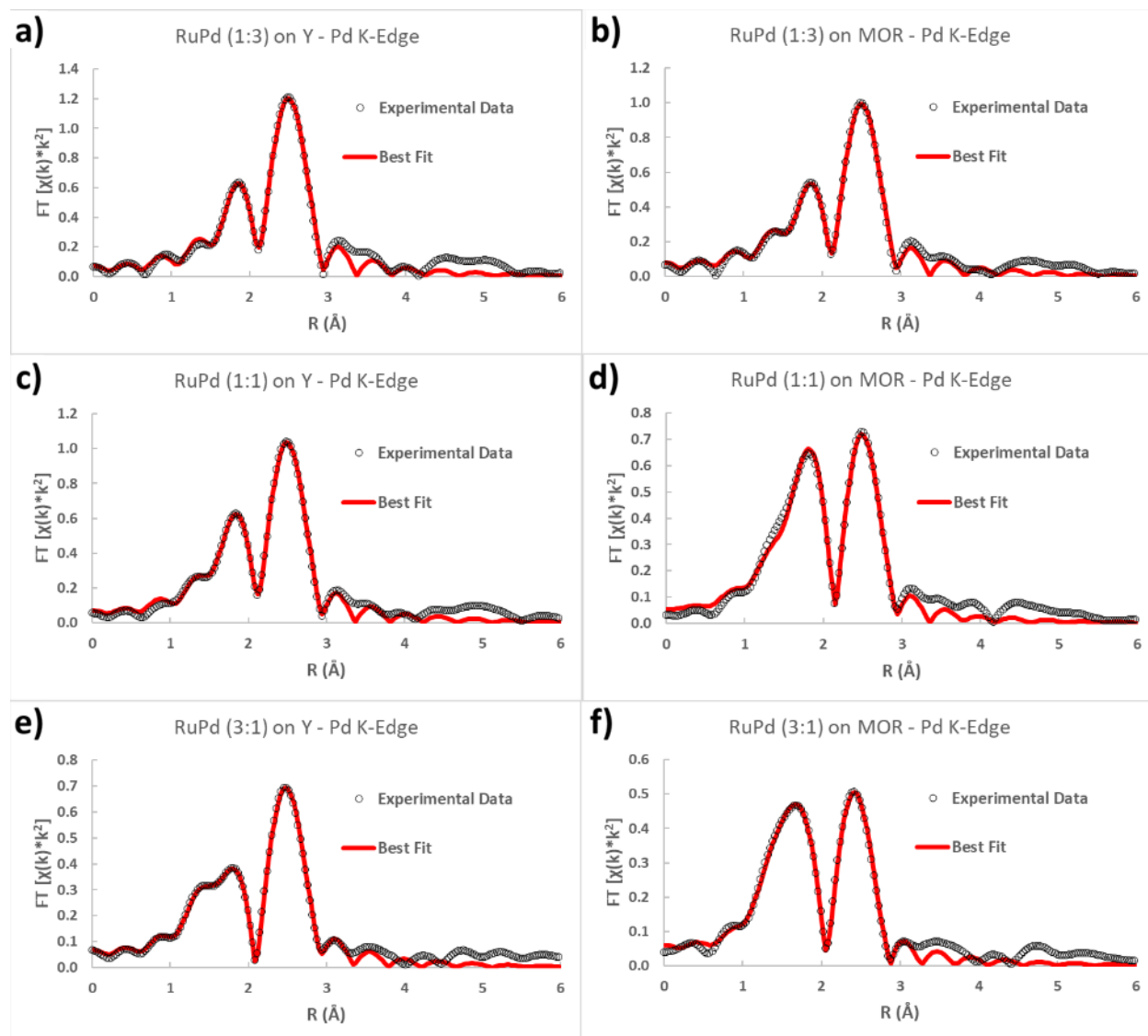
Figure 5-19: Fitted Fourier Transform EXAFS data of bimetallic Ru/Pd (Pd K-Edge) on a) Y (1:3), b) mordenite (1:3), c) Y (1:1), d) mordenite (1:1), e) Y (3:1), and f) mordenite (3:1)

5.4 Conclusion

Close examination of the monometallic ruthenium nanoparticles using XAS analysis revealed that a metal core was unlikely to have formed, with small clusters of ruthenium oxide forming instead, potentially due to oxidation of the nanoparticles or a lack of reduction. This was most prevalent with the Y zeolite, with samples prepared on zeolites beta and mordenite

exhibiting easier formation of a small metal core, as shown by the existence of ruthenium-ruthenium bonding found during EXAFS fitting. When the 3d metal cobalt was introduced into the system, creating a bimetallic sample, very little change could be observed compared to the monometallic series of samples, indicating that the addition of the 3d metal had little effect on the formation of the metal core. The cobalt nanoparticles were likely oxidized during the synthesis, explaining the similar results seen. However, the addition of 4d metal palladium showed a greater amount of metallic character being present in the samples, indicating that the deposited metal nanoparticles remained on the zeolite. XAS analysis of the ruthenium-palladium samples required fitting of all samples, with all scans showing the clear existence of a metal core much larger in size than the cores found in the other two series. Furthermore, adding more palladium compared to ruthenium to the sample, as seen in the samples where palladium was three times more concentrated than ruthenium, resulted in the largest metal cores, indicated by the increasing trends in metal-metal bond distance values for both the Ru and Pd series as the amount of palladium increases. Using XAS analysis, it is possible to determine the bonding properties of the deposited lattice, allowing for greater understanding of the metal on zeolite structure as a whole. Tuning of the metal-metal coordination number and their bond distance shown in this work could be useful for developing new catalysts using metal nanoparticles.

Chapter 6: Conclusions and Future Work

6.1   Conclusions

In this work, the local structural, bonding, and electronic properties of various nanocatalysts were analyzed using XAS. Each study carefully examined a series of samples, and trends seen in the XANES and EXAFS fitting results allowed for a greater understanding of the changes in the atomic and electronic structures of the nanocatalysts.

First, the effect on the electronic structure and bonding properties by doping tungsten into titanium dioxide nanoparticles at various concentrations was examined using XANES and EXAFS analyses, which was complimented by catalytic results obtained in an earlier study. XANES results for the W L_{III}-edge revealed that a clear downward trend of the oxidation state existed as the tungsten concentration increased, with the 2% doped sample having the highest oxidation state (and thus the lowest d electron density). W L_{III}-edge EXAFS results agreed with those from XANES, in which the 2% doped sample had the largest tungsten-oxygen coordination number; unlike the 4% and 10% doped samples, the 2% doped sample had a structure closely resembling that of a TiO_2 unit cell. Ti K-Edge EXAFS analysis revealed that the 4% and 10% samples displayed little difference in their structures. It was determined that replacing Ti with W in the structure of the nanoparticles resulted in Ti vacancies, which, in turn, produced dangling O atoms and O vacancies to act as catalytic sites. Due to the similarity between the structures of TW4 and TW10, as well as the catalytic results, TW4 was the most catalytically active photothermal catalyst.

Next, XANES and EXAFS studies were performed on samples of manganese cobalt oxide nanoparticles supported on carbon nanotubes, with varying concentrations of cobalt and manganese. A clear phase transition of the atomic structure from cubic Co_3O_4 to tetragonal Mn_3O_4 was observed as seen from the fitting analysis trends, which indicated decreases in metal-oxygen coordination and increases in metal-metal bond distances depending on the absorbing element. The sample with an equal ratio of manganese and cobalt, $Mn_{1.5}Co_{1.5}O_4$, showed a dual-phase structure as further revealed using linear combination XANES fitting, where it was determined from both the cobalt and manganese perspectives that the cubic and tetragonal phases existed.

Finally, the analysis of the electronic structure and bonding properties of both monometallic ruthenium nanoparticles and cobalt- or palladium-doped bimetallic ruthenium nanoparticles on zeolite supports was performed. EXAFS analysis clearly showed the lack of metal core formation in the monometallic and bimetallic cobalt series; only in the bimetallic palladium series did a metal core start to form. The fitting results also showed that the choice of zeolite and the concentration of each bimetallic component had a large effect on the size of the metal core, with greater palladium concentrations benefitting metal core formation.

XAS is a powerful tool to study and characterize nanoparticles by closely looking at their electronic properties and local bonding structures. Changes in the content of a nanoparticle sample, such as an increased concentration of a particular element, can result in changes to the local bonding structure. Proper fitting of XAS data allows for the construction of models to visualize the atomic structure of the nanoparticle. The results presented in this work show the advantage of using XAS as a characterization tool to understand the changes within a

nanoparticle's structure. These findings will have potential applications in the design of better nanocatalysts to enhance their catalytic properties.

6.2 Future Work

Future studies on the topics presented in Chapters 3, 4, and 5 could involve a greater number of samples being analyzed to present a clearer trend in data obtained from XAS; in Chapter 4, only three different manganese/cobalt concentrations were analyzed. The synthesis of more samples, such as $Mn_{0.67}Co_{2.33}O_4$, would allow for one to more closely observe changes in the atomic structure; one could also determine at what concentrations a dual-phase structure appears and disappears. In Chapter 5, a larger number of bimetallic metal components (using dopants such as copper, silver, or gold) would be useful to compare to the results already obtained.

In addition, more characterization methods could be used to better support the findings from the XAS analysis. Further TEM imaging of the structures in Chapter 5, which was unable to be performed due to the COVID-19 pandemic, would allow one to see how the nanoparticles are dispersed and their changes in shape. Due to the bimetallic palladium system showing distinct signs of metal core formation, a comparison of their TEM images with those whose systems lack a metal core would show great differences.

Chapter 5 also gives significant detail on the potential of nanoparticles on zeolite supports as nanocatalysts; as such, studies on their catalytic performance must be done. Furthermore, the bimetallic ruthenium/palladium nanoparticles could be tested as potential nanocatalysts for the oxygen evolution reaction, allowing their use in fuel cell catalysis.

References

(1)   Buzea, C.; Pacheco, I. I.; Robbie, K. Nanomaterials and Nanoparticles: Sources and Toxicity. *Biointerphases* **2007**, *2*, MR17.

(2)   Jeevanandam, J.; Barhoum, A.; Chan, Y. S.; Dufresne, A.; Danquah, M. K. Review on Nanoparticles and Nanostructured Materials: History, Sources, Toxicity and Regulations. *Beilstein J. Nanotechnol.* **2018**, *9*, 1050.

(3)   Sukhanova, A.; Bozrova, S.; Sokolov, P.; Berestovoy, M.; Karaulov, A.; Nabiev, I. Dependence of Nanoparticle Toxicity on Their Physical and Chemical Properties. *Nanoscale Res. Lett.* **2018**, *13*, 1.

(4)   Verkhovskii, R.; Kozlova, A.; Atkin, V.; Kamyshinsky, R.; Shulgina, T.; Nechaeva, O. Physical Properties and Cytotoxicity of Silver Nanoparticles under Different Polymeric Stabilizers. *Heliyon* **2019**, *5*, 1.

(5)   Jamkhande, P. G.; Ghule, N. W.; Bamer, A. H.; Kalaskar, M. G. Metal Nanoparticles Synthesis: An Overview on Methods of Preparation, Advantages and Disadvantages, and Applications. *J. Drug Deliv. Sci. Technol.* **2019**, *53*, 101174.

(6)   Reverberi, A. P.; Kuznetsov, N. T.; Meshalkin, V. P.; Salerno, M.; Fabiano, B. Systematical Analysis of Chemical Methods in Metal Nanoparticles Synthesis. *Theor. Found. Chem. Eng.* **2016**, *50*, 59.

(7)   de Oliveira, P. F. M.; Torresi, R. M.; Emmerling, F.; Camargo, P. H. C. Challenges and Opportunities in the Bottom-up Mechanochemical Synthesis of Noble Metal Nanoparticles. *J. Mater. Chem. A* **2020**, *8*, 16114.

(8)   Isaacoff, B. P.; Brown, K. A. Progress in Top-Down Control of Bottom-Up Assembly. *Nano Lett.* **2017**, *17*, 6508.

(9)   Volokitin, Y.; Sinzig, J.; De Jongh, L. J.; Schmidt, G.; Vargaftik, M. N.; Moiseev, I. I. Quantum-Size Effects in the Thermodynamic Properties of Metallic Nanoparticles. *Nature* **1996**, *384*, 621.

(10)   Rioux, R. M.; Song, H.; Hoefelmeyer, J. D.; Yang, P.; Somorjai, G. A. High-Surface-Area Catalyst Design: Synthesis, Characterization, and Reaction Studies of Platinum Nanoparticles in Mesoporous SBA-15 Silica. *J. Phys. Chem. B* **2005**, *109*, 2192.

(11)   Vollath, D.; Fischer, F. D.; Holec, D. Surface Energy of Nanoparticles - Influence of Particle Size and Structure. *Beilstein J. Nanotechnol.* **2018**, *9*, 2265.

(12)   Kelly, K. L.; Coronado, E.; Zhao, L. L.; Schatz, G. C. The Optical Properties of Metal Nanoparticles: The Influence of Size, Shape, and Dielectric Environment. *J. Phys. Chem. B* **2003**, *107*, 668.

(13)   Jana, J.; Ganguly, M.; Pal, T. Enlightening Surface Plasmon Resonance Effect of Metal

Nanoparticles for Practical Spectroscopic Application. *RSC Adv.* **2016**, *6*, 86174.

(14) Azharuddin, M.; Zhu, G. H.; Das, D.; Ozgur, E.; Uzun, L.; Turner, A. P. F.; Patra, H. K. A Repertoire of Biomedical Applications of Noble Metal Nanoparticles. *Chem. Commun.* **2019**, *55*, 6964.

(15) Sankar, M.; He, Q.; Engel, R. V.; Sainna, M. A.; Logsdail, A. J.; Roldan, A.; Willock, D. J.; Agarwal, N.; Kiely, C. J.; Hutchings, G. J. Role of the Support in Gold-Containing Nanoparticles as Heterogeneous Catalysts. *Chem. Rev.* **2020**, *120*, 3890.

(16) Stephen, A. J.; Rees, N. V.; Mikheenko, I.; Macaskie, L. E. Platinum and Palladium Bio-Synthesized Nanoparticles as Sustainable Fuel Cell Catalysts. *Front. Energy Res.* **2019**, *7*, 1.

(17) Creus, J.; De Tovar, J.; Romero, N.; García-Antón, J.; Philippot, K.; Bofill, R.; Sala, X. Ruthenium Nanoparticles for Catalytic Water Splitting. *ChemSusChem* **2019**, *12*, 2493.

(18) Siriwong, C.; Wetchakun, N.; Inceesungvorn, B.; Channei, D.; Samerjai, T.; Phanichphant, S. Doped-Metal Oxide Nanoparticles for Use as Photocatalysts. *Prog. Cryst. Growth Charact. Mater.* **2012**, *58*, 145.

(19) Chavali, M. S.; Nikolova, M. P. Metal Oxide Nanoparticles and Their Applications in Nanotechnology. *SN Appl. Sci.* **2019**, *1*, 1.

(20) Medhi, R.; Marquez, M. D.; Lee, T. R. Visible-Light-Active Doped Metal Oxide Nanoparticles: Review of Their Synthesis, Properties, and Applications. *ACS Appl. Nano Mater.* **2020**, *3*, 6156.

(21) Kuang, L.; Dong, R.; Zhang, Z.; Feng, L.; Wang, F.; Wen, Y. Hydrothermal Synthesis and Metal Ions Doping Effects of Single-Crystal Mn3O4. *Mater. Res. Bull.* **2013**, *48*, 3122.

(22) Djerdj, I.; Arčon, D.; Jagličić, Z.; Niederberger, M. Nonaqueous Synthesis of Metal Oxide Nanoparticles: Short Review and Doped Titanium Dioxide as Case Study for the Preparation of Transition Metal-Doped Oxide Nanoparticles. *J. Solid State Chem.* **2008**, *181*, 1571.

(23) Kumar, M.; Sharma, A.; Maurya, I. K.; Thakur, A.; Kumar, S. Synthesis of Ultra Small Iron Oxide and Doped Iron Oxide Nanostructures and Their Antimicrobial Activities. *J. Taibah Univ. Sci.* **2019**, *13* (1), 280.

(24) Li, Y.; Walsh, A. G.; Li, D.; Do, D.; Ma, H.; Wang, C.; Zhang, P.; Zhang, X. W-Doped TiO 2 for Photothermocatalytic CO 2 Reduction. *Nanoscale* **2020**, 17245.

(25) Bharat, T. C.; Shubham; Mondal, S.; Gupta, H. S.; Singh, P. K.; Das, A. K. Synthesis of Doped Zinc Oxide Nanoparticles: A Review. *Mater. Today Proc.* **2019**, *11*, 767.

(26) Pradeev raj, K.; Sadaiyandi, K.; Kennedy, A.; Sagadevan, S.; Chowdhury, Z. Z.; Johan, M. R. Bin; Aziz, F. A.; Rafique, R. F.; Thamiz Selvi, R.; Rathina bala, R. Influence of Mg Doping on ZnO Nanoparticles for Enhanced Photocatalytic Evaluation and Antibacterial Analysis. *Nanoscale Res. Lett.* **2018**, *13*, 1.

(27) Liu, J.; Prezhdo, O. V. Chlorine Doping Reduces Electron-Hole Recombination in Lead Iodide Perovskites: Time-Domain Ab Initio Analysis. *J. Phys. Chem. Lett.* **2015**, *6*, 4463.

(28) An, L.; Onishi, H. Electron-Hole Recombination Controlled by Metal Doping Sites in NaTaO3 Photocatalysts. *ACS Catal.* **2015**, *5*, 3196.

(29) Yin, Y.; Zhang, X.; Sun, C. Transition-Metal-Doped Fe2O3 Nanoparticles for Oxygen Evolution Reaction. *Prog. Nat. Sci. Mater. Int.* **2018**, *28*, 430.

(30) Miao, Z.; Hu, P.; Nie, C.; Xie, H.; Fu, W.; Li, Q. ZrO2 Nanoparticles Anchored on Nitrogen-Doped Carbon Nanosheets as Efficient Catalyst for Electrochemical CO2 Reduction. *J. Energy Chem.* **2019**, *38*, 114.

(31) Farrusseng, D.; Tuel, A. Perspectives on Zeolite-Encapsulated Metal Nanoparticles and Their Applications in Catalysis. *New J. Chem.* **2016**, *40*, 3933.

(32) Xu, D.; Lv, H.; Liu, B. Encapsulation of Metal Nanoparticle Catalysts within Mesoporous Zeolites and Their Enhanced Catalytic Performances: A Review. *Front. Chem.* **2018**, *6*, 1.

(33) Chai, Y.; Shang, W.; Li, W.; Wu, G.; Dai, W.; Guan, N.; Li, L. Noble Metal Particles Confined in Zeolites: Synthesis, Characterization, and Applications. *Adv. Sci.* **2019**, *6*, 1900299.

(34) Sun, Q.; Wang, N.; Bai, R.; Hui, Y.; Zhang, T.; Do, D. A.; Zhang, P.; Song, L.; Miao, S.; Yu, J. Synergetic Effect of Ultrasmall Metal Clusters and Zeolites Promoting Hydrogen Generation. *Adv. Sci.* **2019**, *6*, 1802350.

(35) Kosinov, N.; Liu, C.; Hensen, E. J. M.; Pidko, E. A. Engineering of Transition Metal Catalysts Confined in Zeolites. *Chem. Mater.* **2018**, *30*, 3177.

(36) Munnik, P.; De Jongh, P. E.; De Jong, K. P. Recent Developments in the Synthesis of Supported Catalysts. *Chem. Rev.* **2015**, *115*, 6687.

(37) Robin, T. F.; Ross, A. B.; Lea-Langton, A. R.; Jones, J. M. Stability and Activity of Doped Transition Metal Zeolites in the Hydrothermal Processing. *Front. Energy Res.* **2015**, *3*, 1.

(38) Visser, T.; Nijhuis, T. A.; Van Der Eerden, A. M. J.; Jenken, K.; Ji, Y.; Bras, W.; Nikitenko, S.; Ikeda, Y.; Lepage, M.; Weckhuysen, B. M. Promotion Effects in the Oxidation of CO over Zeolite-Supported Pt Nanoparticles. *J. Phys. Chem. B* **2005**, *109*, 3822.

(39) De Groot, F. High-Resolution X-Ray Emission and X-Ray Absorption Spectroscopy. *Chem. Rev.* **2001**, *101*, 1779.

(40) Penner-Hahn, J. E. X-Ray Absorption Spectroscopy. *Compr. Coord. Chem. II* **2003**, *2*, 159.

(41) Rehr, J. J.; Albers, R. C. Theoretical Approaches to X-Ray Absorption Fine Structure. *Rev. Mod. Phys.* **2000**, *72*, 621.

(42) Wang, M.; Árnadóttir, L.; Xu, Z. J.; Feng, Z. In Situ X-Ray Absorption Spectroscopy Studies of Nanoscale Electrocatalysts. *Nano-Micro Lett.* **2019**, *11*, 1.

(43) Rodriguez, J. A.; Chaturvedi, S.; Hanson, J. C.; Albornoz, A.; Brito, J. L. Electronic

Properties and Phase Transformations in CoMoO4 and NiMoO4: XANES and Time-Resolved Synchrotron XRD Studies. *J. Phys. Chem. B* **1998**, *102*, 1347.

(44)   Matsuo, S.; Sakaguchi, N.; Wakita, H. Pre-Edge Features of Ti K-Edge X-Ray Absorption near-Edge Structure for the Local Structure of Sol-Gel Titanium Oxides. *Anal. Sci.* **2005**, *21*, 805.

(45)   Sham, T. K. L-Edge x-Ray-Absorption Systematics of the Noble Metals Rh, Pd, and Ag and the Main-Group Metals In and Sn: A Study of the Unoccupied Density of States in 4d Elements. *Phys. Rev. B* **1985**, *31*, 1888.

(46)   Yano, J.; Yachandra, V. K. X-Ray Absorption Spectroscopy. *Photosynth. Res.* **2009**, *102*, 241.

(47)   Rehr, J. J.; Ankudinov, A. L. Progress in the Theory and Interpretation of XANES. *Coord. Chem. Rev.* **2005**, *249*, 131.

(48)   Chiarello, G. L.; Ferri, D. Modulated Excitation Extended X-Ray Absorption Fine Structure Spectroscopy. *Phys. Chem. Chem. Phys.* **2015**, *17*, 10579.

(49)   Ressler, T. WinXAS: A Program for X-Ray Absorption Spectroscopy Data Analysis under MS-Windows. *J. Synchrotron Radiat.* **1998**, *5*, 118.

(50)   Datta, S.; Rule, A. M.; Mihalic, J. N.; Chillrud, S. N.; Bostick, B. C.; Ramos-Bonilla, J. P.; Han, I.; Polyak, L. M.; Geyh, A. S.; Breysse, P. N. Use of X-Ray Absorption Spectroscopy to Speciate Manganese in Airborne Particulate Matter from Five Counties across the United States. *Environ. Sci. Technol.* **2012**, *46*, 3101.

(51)   Antoniak, C. Extended X-Ray Absorption Fine Structure of Bimetallic Nanoparticles. *Beilstein J. Nanotechnol.* **2011**, *2*, 237.

(52)   Mishra, A.; Parsai, N.; Shrivastava, B. D. Simplified Analysis of EXAFS Data and Determination of Bond Lengths. **2011**, *49*, 25.

(53)   Ravel, B.; Newville, M. ATHENA, ARTEMIS, HEPHAESTUS: Data Analysis for X-Ray Absorption Spectroscopy Using IFEFFIT. In *Journal of Synchrotron Radiation*; International Union of Crystallography, 2005; Vol. 12, p 537.

(54)   Rehr, J. J.; Kas, J. J.; Prange, M. P.; Sorini, A. P.; Takimoto, Y.; Vila, F. Ab Initio Theory and Calculations of X-Ray Spectra. *Comptes Rendus Phys.* **2009**, *10*, 548.

(55)   Sun, Y.; Frenkel, A. I.; Isseroff, R.; Shonbrun, C.; Forman, M.; Shin, K.; Koga, T.; White, H.; Zhang, L.; Zhu, Y.; Rafailovich, M. H.; Sokolov, J. C. Characterization of Palladium Nanoparticles by Using X-Ray Reflectivity, EXAFS, and Electron Microscopy. *Langmuir* **2006**, *22*, 807.

(56)   Xu, C.; Huang, W.; Li, Z.; Deng, B.; Zhang, Y.; Ni, M.; Cen, K. Photothermal Coupling Factor Achieving CO2 Reduction Based on Palladium-Nanoparticle-Loaded TiO2. *ACS Catal.* **2018**, *8*, 6582.

(57) Zhou, Y.; Doronkin, D. E.; Zhao, Z.; Plessow, P. N.; Jelic, J.; Detlefs, B.; Pruessmann, T.; Studt, F.; Grunwaldt, J. D. Photothermal Catalysis over Nonplasmonic Pt/TiO2 Studied by Operando HERFD-XANES, Resonant XES, and DRIFTS. *ACS Catal.* **2018**, *8*, 11398.

(58) Tan, T. H.; Scott, J.; Ng, Y. H.; Taylor, R. A.; Aguey-Zinsou, K. F.; Amal, R. Understanding Plasmon and Band Gap Photoexcitation Effects on the Thermal-Catalytic Oxidation of Ethanol by TiO2-Supported Gold. *ACS Catal.* **2016**, *6*, 1870.

(59) Chiang, T. H.; Lyu, H.; Hisatomi, T.; Goto, Y.; Takata, T.; Katayama, M.; Minegishi, T.; Domen, K. Efficient Photocatalytic Water Splitting Using Al-Doped SrTiO3 Coloaded with Molybdenum Oxide and Rhodium-Chromium Oxide. *ACS Catal.* **2018**, *8*, 2782.

(60) Aryanpour, M.; Hoffmann, R.; Disalvo, F. J. Tungsten-Doped Titanium Dioxide in the Rutile Structure: Theoretical Considerations. *Chem. Mater.* **2009**, *21*, 1627.

(61) Couselo, N.; García Einschlag, F. S.; Candal, R. J.; Jobbágy, M. Tungsten-Doped TiO2 vs Pure TiO2 Photocatalysts: Effects on Photobleaching Kinetics and Mechanism. *J. Phys. Chem. C* **2008**, *112*, 1094.

(62) Wang, C.; Chang, F.; Zhang, X.; Zhan, R.; Liu, Y. Minimization of Defects in Nb-Doped TiO2 Photocatalysts by Molten Salt Flux. *Ceram. Int.* **2018**, *44*, 10249.

(63) Muscat, J.; Swamy, V.; Harrison, N. M. First-Principles Calculations of the Phase Stability of TiO2. *Phys. Rev. B - Condens. Matter Mater. Phys.* **2002**, *65*, 2241121.

(64) Choy, J. H.; Kim, D. K.; Hwang, S. H.; Demazeau, G.; Jung, D. Y. XANES and EXAFS Studies on the Ir–O Bond Covalency in Ionic Iridium Perovskites. *J. Am. Chem. Soc.* **1995**, *117*, 8557.

(65) Bak, T.; Li, W.; Nowotny, J.; Atanacio, A. J.; Davis, J. Photocatalytic Properties of TiO2: Evidence of the Key Role of Surface Active Sites in Water Oxidation. *J. Phys. Chem. A* **2015**, *119*, 9465.

(66) Lankauf, K.; Cysewska, K.; Karczewski, J.; Mielewczyk-Gryń, A.; Górnicka, K.; Cempura, G.; Chen, M.; Jasiński, P.; Molin, S. MnxCo3-XO4 Spinel Oxides as Efficient Oxygen Evolution Reaction Catalysts in Alkaline Media. *Int. J. Hydrogen Energy* **2020**, *45*, 14867.

(67) Bobruk, M.; Brylewska, K.; Durczak, K.; Wojciechowski, K.; Adamczyk, A.; Brylewski, T. Synthesis of Manganese-Cobalt Spinel via Wet Chemistry Methods and Its Properties. *Ceram. Int.* **2017**, *43*, 15597.

(68) Li, C.; Han, X.; Cheng, F.; Hu, Y.; Chen, C.; Chen, J. Phase and Composition Controllable Synthesis of Cobalt Manganese Spinel Nanoparticles towards Efficient Oxygen Electrocatalysis. *Nat. Commun.* **2015**, *6*, 1.

(69) Wang, X.; Du, L. Y.; Du, M.; Ma, C.; Zeng, J.; Jia, C. J.; Si, R. Catalytically Active Ceria-Supported Cobalt-Manganese Oxide Nanocatalysts for Oxidation of Carbon Monoxide. *Phys. Chem. Chem. Phys.* **2017**, *19*, 14533.

(70) Li, R.; Hu, D.; Zhang, S.; Zhang, G.; Wang, J.; Zhong, Q. Spinel Manganese-Cobalt Oxide on

Carbon Nanotubes as Highly Efficient Catalysts for the Oxygen Reduction Reaction. *Energy Technol.* **2015**, *3*, 1183.

(71)   Yang, H.; Hu, F.; Zhang, Y.; Shi, L.; Wang, Q. Controlled Synthesis of Porous Spinel Cobalt Manganese Oxides as Efficient Oxygen Reduction Reaction Electrocatalysts. *Nano Res.* **2016**, *9*, 207.

(72)   Zhao, T.; Gadipelli, S.; He, G.; Ward, M. J.; Do, D.; Zhang, P.; Guo, Z. Tunable Bifunctional Activity of MnxCo3–xO4 Nanocrystals Decorated on Carbon Nanotubes for Oxygen Electrocatalysis. *ChemSusChem* **2018**, *11*, 1295.

(73)   Kaewmaraya, T.; Luo, W.; Yang, X.; Panigrahi, P.; Ahuja, R. A New, Layered Monoclinic Phase of Co3O4 at High Pressure. *Phys. Chem. Chem. Phys.* **2015**, *17*, 19957.

(74)   Vila, E.; Rojas, R. M.; Martín De Vidales, J. L.; García-Martínez, O. Structural and Thermal Properties of the Tetragonal Cobalt Manganese Spinels MnxCo3-XO4 (1.4 < x < 2.0). *Chem. Mater.* **1996**, *8*, 1078.

(75)   Chen, J.; Wu, X.; Selloni, A. Electronic Structure and Bonding Properties of Cobalt Oxide in the Spinel Structure. *Phys. Rev. B - Condens. Matter Mater. Phys.* **2011**, *83*, 1.

(76)   Arras, R.; Ly Le, T.; Guillemet-Fritsch, S.; Dufour, P.; Tenailleau, C. First-Principles Electronic Structure Calculations for the Whole Spinel Oxide Solid Solution Range Mn: XCo3- XO4 (0 ≤ x ≤ 3) and Their Comparison with Experimental Data. *Phys. Chem. Chem. Phys.* **2016**, *18*, 26166.

(77)   de Vidales, J. L. M.; Vila, E.; Rojas, R. M.; Garcia-Martinez, O. Thermal Behavior in Air and Reactivity in Acid Medium of Cobalt Manganese Spinels MnxCo3-XO4 (1 ≤ x ≤ 3) Synthesized at Low Temperature. *Chem. Mater.* **1995**, *7*, 1716.

(78)   El Horr, N.; Guillemet-Fritsch, S.; Rousset, A.; Bordeneuve, H.; Tenailleau, C. Microstructure of Single-Phase Cobalt and Manganese Oxide Spinel Mn3-XCoxO4 Ceramics. *J. Eur. Ceram. Soc.* **2014**, *34*, 317.

(79)   Bordeneuve, H.; Tenailleau, C.; Guillemet-Fritsch, S.; Smith, R.; Suard, E.; Rousset, A. Structural Variations and Cation Distributions in Mn3-XCoxO4 (0 ≤ x ≤ 3) Dense Ceramics Using Neutron Diffraction Data. *Solid State Sci.* **2010**, *12*, 379.

(80)   Marei, N. N.; Nassar, N. N.; Vitale, G. The Effect of the Nanosize on Surface Properties of NiO Nanoparticles for the Adsorption of Quinolin-65. *Phys. Chem. Chem. Phys.* **2016**, *18*, 6839.

(81)   Liang, Y.; Wang, H.; Zhou, J.; Li, Y.; Wang, J.; Regier, T.; Dai, H. Covalent Hybrid of Spinel Manganese-Cobalt Oxide and Graphene as Advanced Oxygen Reduction Electrocatalysts. *J. Am. Chem. Soc.* **2012**, *134*, 3517.

(82)   Hu, Y. Z.; Su, Y. T.; Li, C. X.; Li, C. J.; Yang, G. J. Dense Mn1.5Co1.5O4 Coatings with Excellent Long-Term Stability and Electrical Performance under the SOFC Cathode Environment. *Appl. Surf. Sci.* **2020**, *499*, 143726.

(83) Kupchak, I.; Serpak, N. Electronic and Magnetic Properties of Spinel Co3O4 (111) Surface in GGA+U Approximation. *Ukr. J. Phys.* **2017**, *62*, 615.

(84) Guczi, L.; Stefler, G.; Koppny, Z.; Komppa, V.; Reinikainen, M. Co-Ru/NaY Catalyst: Advanced Catalytic System for Selective CO Hydrogénation. *Stud. Surf. Sci. Catal.* **1999**, *121*, 209.

(85) Duchesne, P. N.; Li, Z. Y.; Deming, C. P.; Fung, V.; Zhao, X.; Yuan, J.; Regier, T.; Aldalbahi, A.; Almarhoon, Z.; Chen, S.; Jiang, D. en; Zheng, N.; Zhang, P. Golden Single-Atomic-Site Platinum Electrocatalysts. *Nat. Mater.* **2018**, *17* (11), 1033.

(86) Jung, D.; Lee, S.; Na, K. RuO2 Supported NaY Zeolite Catalysts: Effect of Preparation Methods on Catalytic Performance during Aerobic Oxidation of Benzyl Alcohol. *Solid State Sci.* **2017**, *72*, 150.

(87) Zahmakiran, M.; Özkar, S. Zeolite Confined Nanostructured Dinuclear Ruthenium Clusters: Preparation, Characterization and Catalytic Properties in the Aerobic Oxidation of Alcohols under Mild Conditions. *J. Mater. Chem.* **2009**, *19*, 7112.

(88) Zahmakiran, M.; Özkar, S. Zeolite-Confined Ruthenium(0) Nanoclusters Catalyst: Record Catalytic Activity, Reusability, and Lifetime in Hydrogen Generation from the Hydrolysis of Sodium Borohydride. *Langmuir* **2009**, *25*, 2667.

(89) Ajellal, N.; Carpentier, J. F.; Guillaume, C.; Guillaume, S. M.; Helou, M.; Poirier, V.; Sarazin, Y.; Trifonov, A. Metal-Catalyzed Immortal Ring-Opening Polymerization of Lactones, Lactides and Cyclic Carbonates. *Dalt. Trans.* **2010**, *39*, 8363.

(90) Mishra, D. K.; Dabbawala, A. A.; Park, J. J.; Jhung, S. H.; Hwang, J. S. Selective Hydrogenation of D-Glucose to d-Sorbitol over HY Zeolite Supported Ruthenium Nanoparticles Catalysts. *Catal. Today* **2014**, *232*, 99.

(91) Guczi, L.; Bazin, D. Structure and Selectivity of Metal Catalysts: Revisiting Bimetallic Zeolite Systems. *Appl. Catal. A Gen.* **1999**, *188*, 163.

(92) Taufiqurrahmi, N.; Mohamed, A. R.; Bhatia, S. Nanocrystalline Zeolite Y: Synthesis and Characterization. *IOP Conf. Ser. Mater. Sci. Eng.* **2011**, *17*, 1.

(93) Hao, W.; Zhang, W.; Guo, Z.; Ma, J.; Li, R. Mesoporous Beta Zeolite Catalysts for Benzylation of Naphthalene: Effect of Pore Structure and Acidity. *Catalysts* **2018**, *8*, 1.

(94) Kumar, M.; Berkson, Z. J.; Clark, R. J.; Shen, Y.; Prisco, N. A.; Zheng, Q.; Zeng, Z.; Zheng, H.; McCusker, L. B.; Palmer, J. C.; Chmelka, B. F.; Rimer, J. D. Crystallization of Mordenite Platelets Using Cooperative Organic Structure-Directing Agents. *J. Am. Chem. Soc.* **2019**, *141*, 20155.

(95) Cheng, K.; Kang, J.; Huang, S.; You, Z.; Zhang, Q.; Ding, J.; Hua, W.; Lou, Y.; Deng, W.; Wang, Y. Mesoporous Beta Zeolite-Supported Ruthenium Nanoparticles for Selective Conversion of Synthesis Gas to C 5-C 11 Isoparaffins. *ACS Catal.* **2012**, *2*, 441.

(96) Mishra, D. K.; Dabbawala, A. A.; Hwang, J. S. Ruthenium Nanoparticles Supported on

Zeolite y as an Efficient Catalyst for Selective Hydrogenation of Xylose to Xylitol. *J. Mol. Catal. A Chem.* **2013**, *376*, 63.

(97)   Yao, Q.; Lu, Z. H.; Yang, K.; Chen, X.; Zhu, M. Ruthenium Nanoparticles Confined in SBA-15 as Highly Efficient Catalyst for Hydrolytic Dehydrogenation of Ammonia Borane and Hydrazine Borane. *Sci. Rep.* **2015**, *5*, 1.

(98)   Wang, L. L.; Khare, S. V.; Chirita, V.; Johnson, D. D.; Rockett, A. A.; Frenkel, A. I.; Mack, N. H.; Nuzzo, R. G. Origin of Bulklike Structure and Bond Length Disorder of Pt37 and Pt6Ru31 Clusters on Carbon: Comparison of Theory and Experiment. *J. Am. Chem. Soc.* **2006**, *128*, 131.

(99)   Bazin, D.; Kovács, I.; Lynch, J.; Guczi, L. Ru-Co/NaY Bimetallic Catalysts: In Situ EXAFS Study at Co K- and Ru K-Absorption Edges. *Appl. Catal. A Gen.* **2003**, *242*, 179.

(100)   Guczi, L.; Sundararajan, R.; Koppány, Z.; Zsoldos, Z.; Schay, Z.; Mizukami, F.; Niwa, S. Structure and Characterization of Supported Ruthenium-Cobalt Bimetallic Catalysts. *J. Catal.* **1997**, *167*, 482.

(101)   Reksten, A. H.; Russell, A. E.; Richardson, P. W.; Thompson, S. J.; Mathisen, K.; Seland, F.; Sunde, S. Strategies for the Analysis of the Elemental Metal Fraction of Ir and Ru Oxides: Via XRD, XANES, and EXAFS. *Phys. Chem. Chem. Phys.* **2019**, *21*, 12217.

(102)   Shah, R.; Payne, M. C.; Lee, M.; Gale, J. D. Understanding the Catalytic Behavior of Zeolites : A First-Principles Study of the Adsorption of Methanol. *Science.* **1996**, *271*, 1395.

(103)   Veerakumar, P.; Salamalai, K.; Dhenadhayalan, N.; Lin, K. C. Catalytic Activity of Bimetallic (Ruthenium/Palladium) Nano-Alloy Decorated Porous Carbons Toward Reduction of Toxic Compounds. *Chem. - An Asian J.* **2019**, *14*, 2662.

(104)   Wu, D.; Kusada, K.; Kitagawa, H. Recent Progress in the Structure Control of Pd–Ru Bimetallic Nanomaterials. *Sci. Technol. Adv. Mater.* **2016**, *17*, 583.